8-14-2023

Multi-color Fluorescent Microscopy and Deep Learning for Studying Eukaryotic Organelles: Unveiling Cellular Growth in a System Biology Perspective

Shixing Wang
Washington University in St. Louis

WASHINGTON UNIVERSITY IN ST. LOUIS

Department of Physics

Dissertation Examination Committee:
Shankar Mukherji, Chair
Anders Carlsson
David Kast
Ralf Wessel
Chong Zu

Multi-color Fluorescent Microscopy and Deep Learning for Studying Eukaryotic Organelles:

Unveiling Cellular Growth in a System Biology Perspective

by

Shixing Wang

A dissertation presented to
Washington University in St. Louis
in partial fulfillment of the
requirements for the degree
of Doctor of Philosophy

August 2023
St. Louis, Missouri

Table of Contents

List of Figures

List of Tables

Acknowledgments

First and foremost, I would like to extend my sincere gratitude to my supervisor, Shankar Mukherji, for his unwavering support, expertise, and dedication. Their guidance, constructive feedback, and insightful discussions have been instrumental in shaping the direction and quality of this research work. I am truly grateful for their mentorship, which has been invaluable to my personal and academic growth.

I am grateful to the members of my thesis committee, Anders Carlsson, David Kast, Ralf Wessel, and Chong Zu, for their time, expertise, and valuable feedback during the various stages of my research. Their insightful comments and suggestions have immensely contributed to the overall improvement of this thesis.

I would like to extend my thanks to my colleagues and friends for their support and encouragement, especially Kiandokht Panjtan Amiri, Luis Perez, Aline Arra, Anang Singh, and many other talented ones. Their camaraderie, intellectual discussions, and shared experiences have made this journey enjoyable and memorable.

Last but not least, I would like to express my heartfelt appreciation to the faculty and staff of the Department of Physics at Washington University in St. Louis.

Shixing Wang

Washington University in St. Louis

August 2023

Dedicated to my grandfather.

ABSTRACT OF THE DISSERTATION

Multi-color Fluorescent Microscopy and Deep Learning for Studying Eukaryotic Organelles: Unveiling Cellular Growth in a System Biology Perspective

by

Shixing Wang

Doctor of Philosophy in Physics

Washington University in St. Louis, 2023

Professor Shankar Mukherji, Chair

Eukaryotic cells are building blocks to complex living systems, characterized by membrane-bound organelles. Studying how eukaryotic organelles react to cellular growth and size increase is crucial, but it demands biochemical and biophysical manipulations, as well as quantitative observation tools in microscopy. We developed a multi-color yeast strain with tagged fluorescent proteins, enabling systematic measurements of 6 organelles inside each cell using spectral confocal microscopy. These measurements provided insights into how organelle biogenesis is coordinated with cellular size and growth rate regulation via different signaling pathways. To explore cellular growth under dynamic conditions, I utilized deep learning for organelle recognition using low-power bright field fluorescent microscopy. This technique maintains high spectral resolution while minimizing photodamage and enabling timelapse acquisition. Training output statistics demonstrated excellent fidelity to the target. The work in this thesis lays a foundation for capturing how organelle dynamics and cellular growth interrelate.

Chapter 1: Introduction

The hierarchy of biological organizations is a fundamental concept in the field of biology that describes the nested levels of complexity found in living systems. From the smallest building blocks of life to the intricate functioning of ecosystems, this hierarchical structure provides a framework for understanding the organization and interactions within biological systems. At the lowest level, molecules and macromolecules combine to form cells, which are the basic units of life. Cells then organize into tissues, which in turn form organs that carry out specific functions within organisms. Multiple organs working together comprise organ systems, enabling the coordination of complex physiological processes. At the next level, organisms, whether unicellular or multicellular, represent individual living entities capable of growth, reproduction, and adaptation. Populations consist of groups of organisms of the same species living in a defined area, while communities include various populations interacting within an ecosystem. Finally, ecosystems encompass all living organisms and their interactions with the physical environment, forming a dynamic and interconnected web of life [1].

Eukaryotic cells are characterized by their compartmentalization into organelles, which are specialized structures that carry out specific functions. The coordinated biogenesis of organelles is essential for cell growth and differentiation [1]. In recent years, there has been growing interest in understanding the mechanisms that regulate organelle biogenesis.

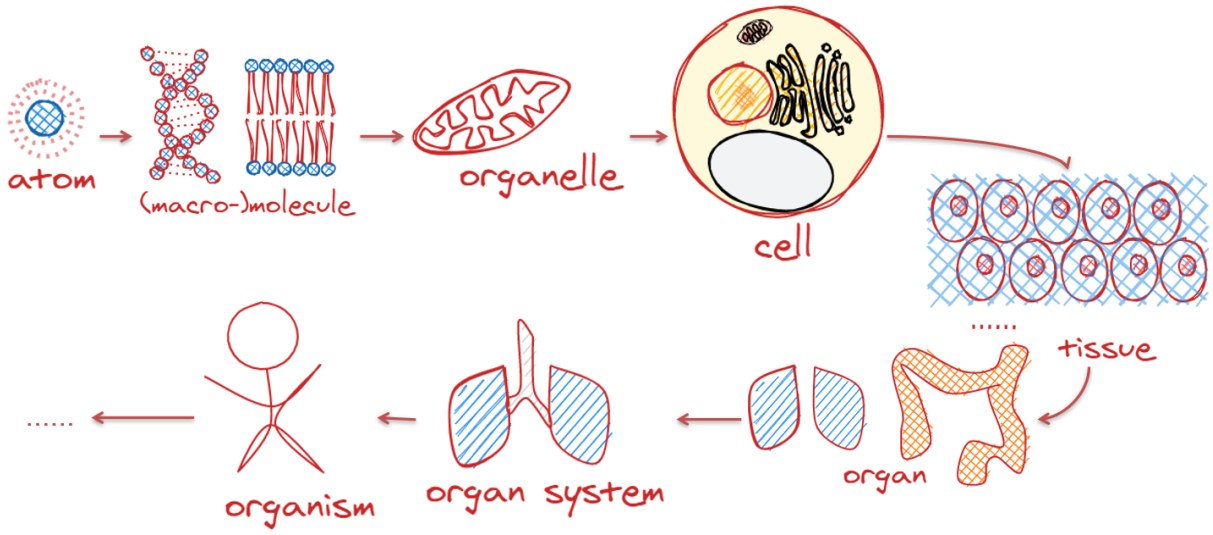

Figure 1 hierarchy of biological organizations

Chan YH et. al reviews the various ways in which cells can sense and control the size of their organelles, such as stereotyped growth, allometric growth, and fixed-precursor recruitment [2]. Levy DL et. al discusses the mechanisms of intracellular scaling, which is the process by which cells adjust their size and shape in response to environmental and internal cues. Cell sizes are positively correlated to genome size. Nuclear size is coupled with the cell so that the ratio of nuclear over cytoplasm is maintained. This is achieved by nuclear import, contributed by nuclear pore complexes [3]. Goehring NW and Hyman AA investigate a group of mechanisms that regulate organelle growth by primarily utilizing the cytoplasm as a restricted reservoir of available material. The increase in the size of cytoplasm could provide more building units for cell components, while the decreased concentration of the units serves as negative feedback [4]. Jorgensen P and colleges also found the consistency of nuclear volume fraction to the cell. This nuclear size maintenance does not require continuous biogenesis of ribosome or its export into the cytoplasm [5]. Mukherjee RN et. al found that the perinuclear endoplasmic reticulum serves

as the limiting pool for nuclear surface growth [6]. Chan YH, and Marshall WF measured the vacuole size, and found that both its volume and surface area scale with the cell. They also proposed a model for the size scaling of vacuole given cell and vacuole growth rates [7]. The size of mitochondrial network has also been found to scale with the size of the budding yeast [8, 9]. New budding yeast cells get mitochondria of similar ratio, while aged mother cells keep decreasing their mitochondrion volume fraction [8]. This is achieved mainly through fission and fusion of mitochondria [9]. These researches provide important knowledge of the scaling of cells and organelles, but they are mainly with respect to pairs of organizations, and we still lack system level insights.

The interaction between organelles is also of great interest, but such efforts are limited due to technical difficulties to measure multiple interactions simultaneously, historically disproportionate interest in cancer-related studies, the immerse scale of commitment, and complexity of biological models to understand them [10]. There have been heavily data-driven studies in omics, but to our knowledge, such analysis has not been applied on the interactions between organelles.

This thesis investigates three aspects of organelle biogenesis in yeast cells: (1) the correlation structure of systems-level organelle biogenesis with cellular growth [11], (2) a quantitative model to explain the non-trivial observations and the experimental verification [12], and (3) the use of deep learning to segment and identify organelles.

The first project uses a strain of Saccharomyces cerevisiae called "rainbow yeast" that allows simultaneous visualization of the six major metabolically active organelles. Hyperspectral imaging of thousands of single rainbow yeast cells revealed that the systems-level organelle biogenesis program is composed of collective organelle modes activated by changes in nutrient availability. Chemical biological dissection suggests that the sensed growth rate and size of the cell specifically activate these distinct organelle modes, which combine to mount the cellular organelle-scale response to environmental cues. Mathematical modeling and synthetic biological control of cytoplasmic availability suggests that distinct organelle modes allow the cell to maintain robust growth homeostasis in constant environments while remaining responsive to changes across diverging environments [11].

We developed a quantitative model where the cell detects changes in its volume and assigns excess volumes to vacuoles in order to maintain a consistent nucleocytoplasmic volume fraction. To test this hypothesis, a synthetic biological condensate called PopTag, derived from Caulobacter crescentus, was used to artificially increase cytoplasmic crowding. The results supported the concept that the cell differentiates the response of organelles to cell size and growth rate [12].

The third project uses a deep learning model called U-Net to segment and identify organelles in yeast cells. The model was trained on a dataset of confocal microscopy images, and it was able

to accurately segment and identify peroxisomes and endoplasmic reticulum structures. However, the recognition of vacuoles was hindered by the limitations posed by the low signal-to-noise ratio in both the training inputs and targets.

The findings of this thesis provide new insights into the mechanisms that regulate organelle biogenesis in yeast cells. The results of the first project suggest that the cell uses a complex regulatory network to coordinate the biogenesis of different organelles in response to changes in environmental conditions. The results of the second project demonstrate the potential of deep learning for segmenting and identifying organelles in yeast cells.

Chapter 2: Reaction of Eukaryotic Organelles to Cellular Growth And Size Increase

2.1 Introduction

The spatial compartmentalization of organelles is a prominent feature that distinguishes eukaryotic cells [1]. A fundamental objective in cell biology is to comprehend the coordinated biogenesis of organelles on a systems scale, building upon the achievements in uncovering comparable "growth laws" in prokaryotic systems [2] [3] [4] [13]. However, our understanding of the physiological principles governing the quantitative management of organelle growth in cells remains limited. This limitation primarily arises from the challenge of ensuring sufficient statistical power to assess theoretical frameworks for interpreting such findings [4] [14] [15] [16].

The coordination of organelle growth with overall cellular growth has predominantly been investigated through scaling relationships between organelle sizes and the sizes of their host cells. For instance, it is widely recognized that the volume of the nucleus exhibits linear scaling with the size of the host cell [5]. Similar scaling relationships have been observed for other organelles such as the endoplasmic reticulum [6], vacuoles/lysosomes [7, 17], and mitochondria [8, 9]. However, our knowledge regarding pairwise scaling relationships among organelles remains limited, and even [18] less characterized are the interactions among multiple organelles that play a crucial role in regulating cellular physiology at different scales. The obstacle against

such insights mainly lies in the difficulty to simultaneously measure multiple organelles within the same cell.

To enable the visualization of the six primary organelles in budding yeast, we employed a strategy involving the transcriptional fusion of genes encoding fluorescent proteins to genes encoding organelle-resident proteins that have been well-established to localize specifically to a particular organelle [18, 19]. The rainbow yeast cells were cultured and imaged using a confocal laser-scanning microscope with a diffraction grating that has spectral resolvability. We applied straightforward data reduction methods that yielded profound insights into the coupling between organelle biogenesis and the interconnected variables of cell growth rate and cell size.

2.2 Methods

2.2.1 Construction of Multiple Fluorescence Labelled Yeast Strains

"EYrainbow"

To generate a diploid strain of Saccharomyces cerevisiae that labels six organelles, we employed a mating strategy between the two haploid strains, EY2795 and EY2796. Each haploid strain was consecutively tagged with three organelles by integrating a fluorescent protein gene before the stop codon of the gene localized to the respective organelle. The plasmids used for tagging contained the template sequence for the fluorescent protein and selection marker, the gene expressed in the organelle, and the haploid strain that the fluorescent protein gene was

transformed into. Table 1 provides detailed information on the template plasmids used for each organelle.

To integrate mCherry-TRP and mtagBFP2-TRP into the yeast genome, we linearized the respective plasmids and transformed them into the yeast. The remaining fluorescent protein genes were obtained via PCR, using sequence-specific primers designed with a forward primer containing 40 bases upstream of the stop codon of the organelle-specific gene and the beginning 20 bases of the fluorescent protein gene. The reverse primer contained the reversed complementary sequence of 20 bases of the marker stop codon on the template plasmid and 40 base pairs downstream of the stop codon of the organelle-specific gene. The transformed cells were selected on dropout or antibiotic plates according to the selection markers. Furthermore, we custom synthesized the mTFP1 sequence and inserted it into a PKT backbone with a KAN marker. Then the customized plasmids were transformed into the corresponding haploid strains and selected according to the markers. After each haploid had been verified to have 3 fluorescent proteins, they were crossed on a SD-Ura+G418 selection plate. The survived colonies consisted of diploid strains with 6 fluorescent proteins.

Haploid	Organelle	Localized Gene	Fluorescent Protein	Selection Marker	Template Plasmid	Addgene #
EY2795	**vacuole**	**VPH1**	**mTFP1**	**KAN**	**customized PKT**	**n/a**
EY2795	**Golgi apparatus**	**SEC7**	**mCitrine**	**HIS**	**pKT0211** [20]	**#8734**
EY2795	**lipid droplet**	**ERG6**	**mCherry**	**TRP**	**ZJOM70** [21]	**#133658**
EY2796	**peroxisome**	**C-SKL**	**mtagBFP2**	**TRP**	**ZJOM160** [21]	**#133670**
EY2796	**endoplasmic reticulum**	**SEC61**	**superfolderGFP**	**URA**	**pFA6a-link-yoSuperfolderGFP-CaURA3** [22]	**#44873**
EY2796	**mitochondrion**	**TOM70**	**tdTomato**	**HIS**	**pFA6a-link-tdTomato-SpHis5** [22]	**#44640**

Table 1 In each yeast haploid strain, the correspondence across the tagged organelles, selected localized protein, fluorescent protein tags, selection markers, and template plasmids containing the fluorescent proteins and the markers.

"EYrainbowWhi5Up"

In order to perturb the size of the yeast cells, we tuned up the expression level of Whi5, a known repressor of G1 transcription [23]. Cells that express more Whi5 will stay longer during G1 phase, producing more intracellular materials and grow bigger in size. The Whi5 overexpression plasmid went through PCR with forward and backward primers homologous to the designed insertion site. Then the PCR products were transformed into the EY2795 and EY2796 haploids that each has 3 fluorescent protein tags. Then the haploids were crossed on a selection plate to get the Whi5 overexpression diploids with 6 fluorescent proteins, namely the "EYrainbowWhi5Up" strain.

2.2.2 Strain Storage, Cultivation, and Nutrition Perturbation

Table 3 provides a list of the different media used in our experiments. Prior to each experiment, the yeast cells were transferred from the petri dish to 10 mL of SD complete media and allowed to grow overnight in a thermostatic shaker.

For the Whi5 overexpression experiment, 10 μM of beta estradiol was added to the experimental group, and the cells were grown in the shaker overnight before microscopy imaging.

For all other experiments, the overnight culture was diluted to an optical density of OD (600 nm) = 0.1 in SD complete media and grown in the shaker for 2 hours to resume exponential growth. The cells were then washed twice and transferred into the respective experimental media. After

three hours of growth in the experimental media, the cells were harvested and observed under the microscope.

Organelles	Excitation wavelength	Detecting wavelength	Spectral resolution
peroxisome & vacuole	455 nm	460 nm – 510 nm	10 nm
endoplasmic reticulum	488 nm	500 nm – 550 nm	50 nm
Golgi apparatus	514 nm	520 nm – 558 nm	38 nm
mitochondrion & lipid droplet	561 nm	567 nm – 647 nm	10 nm

Table 2 Optical configurations to observe different (combinations of) organelles with the spectral confocal fluorescent microscopy

2.2.3 Fluorescent Hyperspectral Confocal Microscopy Imaging

Harvested cells from the experimental media were used to prepare microscope slides for imaging, which were observed under a Nikon Ti2 microscope. Image acquisition began once the cells had stopped moving within the field of view. A bright field microscopy image of the focal plane was captured first. Subsequently, hyper-spectral confocal microscopy images were captured at four different optical configurations, as detailed in Table 3. Following the acquisition of the z-stack images, another single-z bright field microscopy image was captured slightly off focus to facilitate cell segmentation during image analysis.

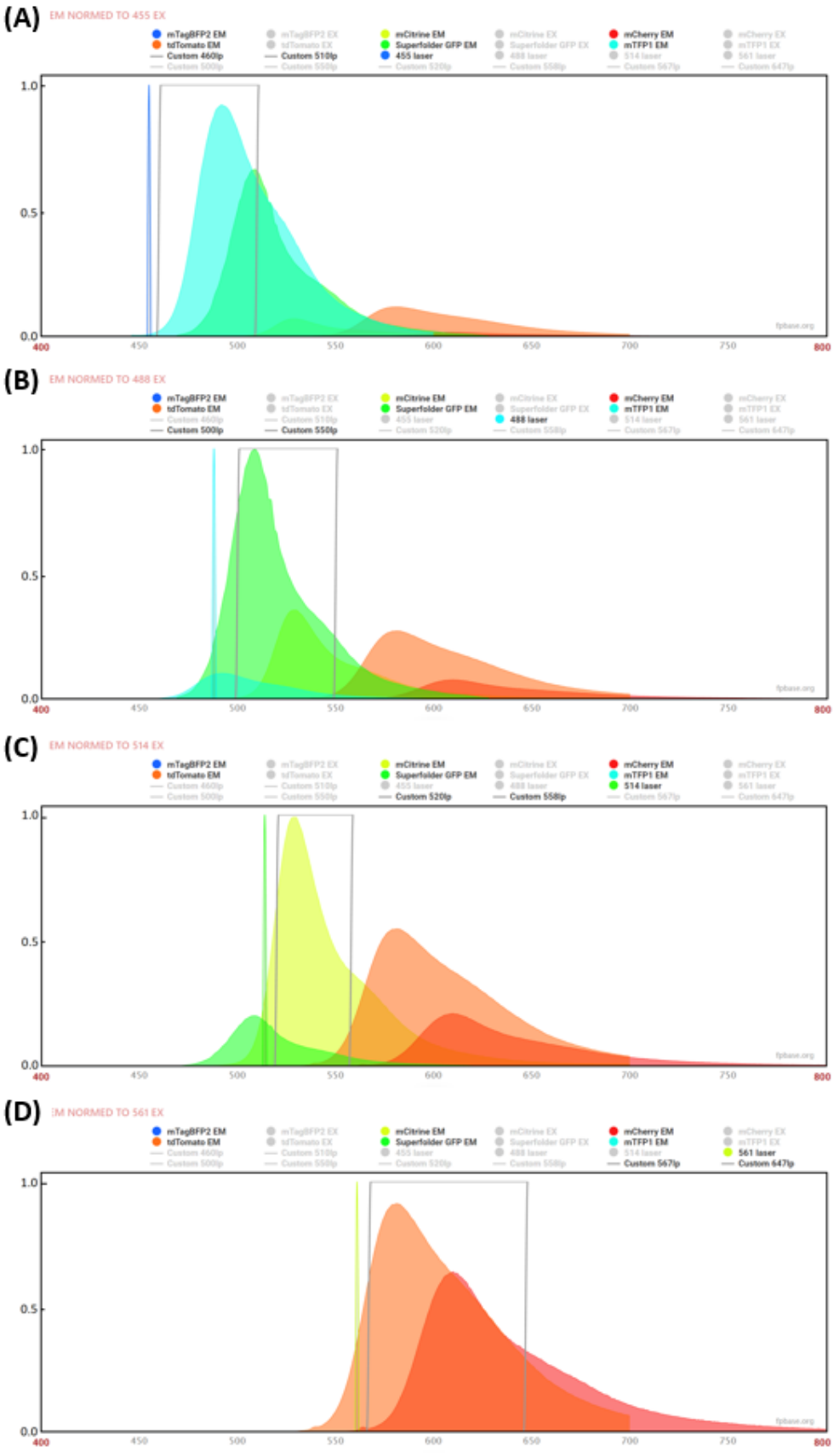
(A)
EM NORMED TO 455 EX
mTagBFP2 EM
tdTomato EM
Custom 460/lp
Custom 500/lp
mTagBFP2 EX
tdTomato EX
Custom 510/lp
Custom 550/lp
mCitrine EM
Superfolder GFP EM
455 laser
Custom 520/lp
mCitrine EX
Superfolder GFP EX
488 laser
Custom 558/lp
mCherry EM
mTFP1 EM
514 laser
Custom 567/lp
mCherry EX
mTFP1 EX
561 laser
Custom 647/lp
1.0
0.5
0.0
400
450
500
550
600
650
700
750
800
fpbase.org
(B)
EM NORMED TO 488 EX
488 laser
(C)
EM NORMED TO 514 EX
514 laser
Custom 520/lp
Custom 558/lp
(D)
EM NORMED TO 561 EX
561 laser
Custom 567/lp
Custom 647/lp

Figure 2 Emission spectra of the 6 fluorescent proteins, normalized by the laser light sources in the 4 optical configurations. (**A**) peroxisome & vacuole (**B**) endoplasmic reticulum (**C**) Golgi apparatus (**D**) mitochondrion & lipid droplet. The sharp colored peak labels the laser light wavelengths. The grey boxes label the scanning wavelength range of the spectral detector in each optical configuration. The data are from FPbase **[24]**.

2.2.4 Image Processing

We utilized scikit-image [25], a Python-based image processing package, alongside YeaZ [26], a convolutional neural network specifically designed for yeast cellular segmentation, to segment the cells. Bright field microscopy images were first registered from the bright field camera to the hyper-spectral detector, and then underwent histogram equalization filtering prior to being fed into YeaZ for segmentation. The resulting segmentations from the before- and after- images were manually compared, and cells that moved during image acquisition were subsequently excluded. In the experiment involving leucine, since bright field images were not taken, segmentation was instead performed on the average z-projection of the green channel 2 hyperspectral confocal microscopy images via manual thresholding and watershed using ImageJ [27].

To obtain single-channel z-stack images of individual organelles, we demixed the blue and red channels of hyper-spectral confocal microscopy images using the Nikon Ti2 Analysis software. Spectral characteristics were manually extracted by selecting regions of interest, and the resulting single-organelle images were then passed through ilastik [28], an interactive machine learning software, for segmentation. Prior to inputting the images into ilastik, the yellow and red channel images underwent cleaning via the subtraction of the average pixel intensity of the surrounding neighborhood of each cell, followed by the application of a 3D Gaussian filter with

sigma=0.75 to all images. An ilastik project was then trained for each organelle using hand-drawn foreground-background labels on a sample image.

The binary images generated by ilastik were subsequently post-processed based on the type of organelle contained within. For small and globular organelles such as the peroxisome, the Golgi apparatus, and the lipid droplet, the binary images underwent watershed using the Gaussian images as references. For the endoplasmic reticulum, the binary images were skeletonized, while for mitochondria, the binary images were labeled by treating simply connected pixels as individuals. For the vacuole, the binary images were processed slice by slice over the z-stack, with each z-plane first being skeletonized, then having its background flood filled, and finally having its color reversed so that the foreground represents the cross-section of the vacuole in that plane.

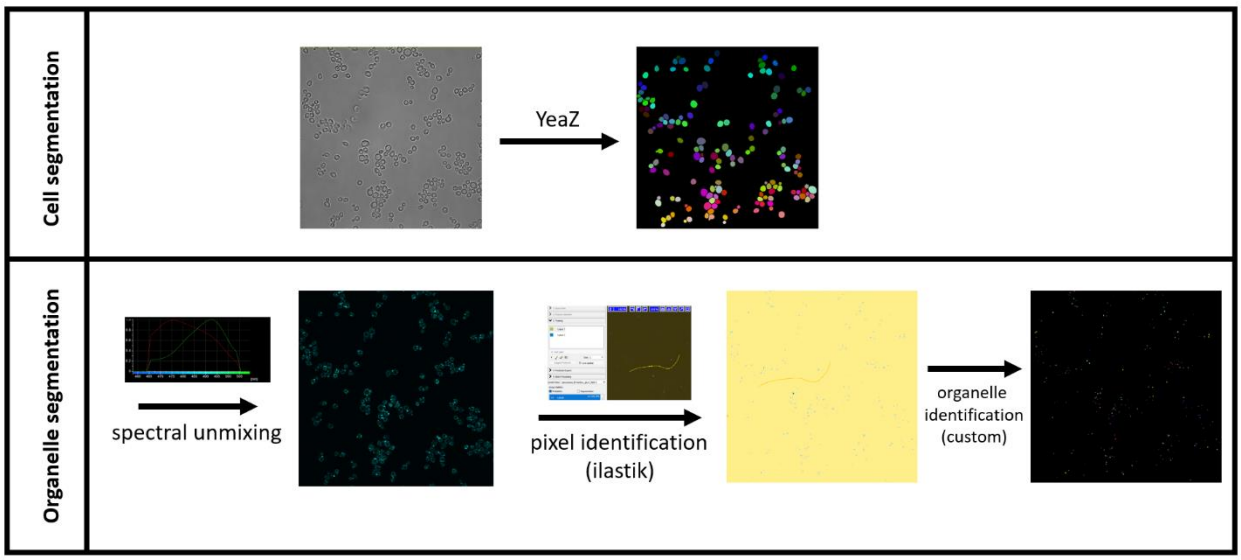

Figure 3 Schematic illustrating the sequential steps in image processing for cell and organelle segmentation.

Top row: the brightfield cell image segmentation process using the YeaZ method (REF). The left panel shows the raw brightfield image, while the right panel presents the mask of segmented cells identified by YeaZ. **Bottom row**: showcases the segmentation of fluorescent organelle images. The first step involves spectral unmixing of hyperspectral image data into individual organelle channels The second step entails training the ilastik tool to differentiate between background and fluorescence-containing pixels for automated pixel classification. Finally, the third step involves grouping neighboring pixels to form structures representing organelles.

To obtain organelle statistics for different cells, we iterated over the cells in the segmented cell image for each field of view and labeled and measured the area of each cell. We then applied the cell mask to each organelle image across all z planes. For organelles other than the vacuole, we recorded the label and number of pixels for each label in the image. For the vacuole, we iterated over the z-planes, identified the disk with the largest cross-section area, and recorded its statistics. The volumes of cells and vacuoles were estimated by treating the organism as a cylinder with a height equal to its diameter, while non-organelle volumes were estimated by subtracting the six organelle volumes from the cellular volumes.

2.2.5 Data Analysis

Validation of the Spectral Unmix

To validate the unmixing of the spectral confocal microscopy image, we selected the pixels from the machine-learning based segmentation images, and examined the spectra of the pixels in the corresponding spectral images.

In the images that contain peroxisomes and vacuoles, and images containing mitochondria and lipid droplets, we picked regions of interest (ROIs) that belongs to the specific organelles

according to our knowledge of their morphology, and obtained the spectra in those pixels as the benchmark. Then we normalized the spectra with respect to the channel with the highest intensity. The normalized spectra were averaged over all pixels from the same experiment, and plotted along with the benchmark spectra.

As for endoplasmic reticulum and Golgi apparatus, we took the non-spectral confocal microscopy images in our experiments. In order to validate that these two organelles would not show up in the images of the other organelle, we took the spectral confocal images over the same wavelength ranges, namely green and yellow ranges. The organelles were segmented with machine-learning based ilastik. Then we checked the spectra of the pixels that belong to both organelles in green and yellow spectral images. Both of the spectra in each image were normalized with respect to the maximum channel from the brighter spectra in that image.

Error Analysis of the Organelle Segmentation

To assess the error in organelle size resulting from segmentation, we utilized the "probability" output generated by ilastik. To perform the foreground-background segmentation, we identified pixels whose foreground probability exceeded 0.5 as belonging to organelles. We then extracted all unique values present in the probability tensor. The upper error pixels were defined as those with a probability equal to the lowest value greater than 0.5, while the lower pixels were those with a probability equal to the highest value less than 0.5. In the case of the peroxisome-vacuole images from the leucine experiment, we used a threshold of 0.33 for both channels. The ratios of

the upper and lower errors over the total volumes of different organelles are presented in Figure 6.

Correlation Coefficient of Organelle Properties

We first grouped data by experiments. Within each experiment, we grouped the organelle property data by the cells to which they belonged and calculated the average volumes, total volumes, and counting numbers of organelles within each cell. For each cell, we also computed three statistics for the six organelles (excluding the counting number of the endoplasmic reticulum) and cellular properties, including the cross-section area, estimated volume, and characteristic length (i.e., the estimated radii of the cross-section). We then calculated the correlation coefficients between each pair of statistical variables.

Log-log Regression of the Cell/Organelle Total Volume

The organelle property data were collected and grouped by individual cells to obtain the total volume of each type of organelle. The cellular volumes, six organelle volumes, and non-organelle volumes were then transformed by taking their logarithms. To reduce statistical fluctuations, we excluded the smallest 10% of volumes for each experiment. We performed a linear regression analysis for each pair of logarithms, and recorded the slope in an 8x8 matrix. We also created a scatter plot of the logarithms in an 8x8 grid, where each experiment condition was labeled with a different color.

Principal Component Analysis and Projection of Condition Vectors

The data were grouped by experiments. Within each experiment, the individual cells were kept as the rows of the data table, while the volume fractions of the six organelles were kept as the columns. The principal component analysis (PCA) was performed using scikit-learn, a python-based machine learning tool library. Conceptually PCA is the singular value decomposition of the cross-variance matrix of the original data table. The eigenvectors of the cross-variance matrix are the principal vectors, while the eigenvalues are proportional to the variance explained by the eigenvectors.

The 6-dimensional volume fraction vectors of individual cells can be linearly expressed by the principal components. For the cells that appeared in each experimental condition, we averaged their coordinates in the PCA space to get a centroid. Then the centroids were regressed to a straight line. We compared the direction of this line with the principal components by calculating the inner product between the direction vector and the principal components.

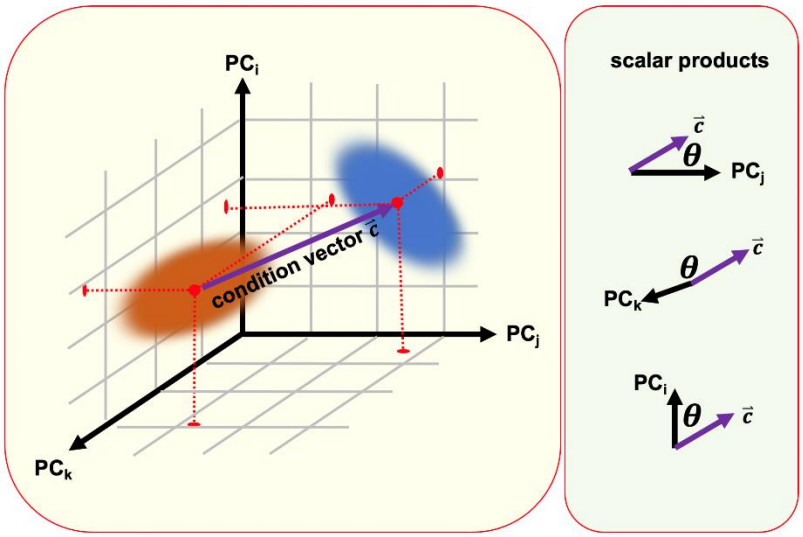

Figure 4 Schematic depiction of the condition vector in the PCA space.

2.3 Results

2.3.1 Validation on Spectral Unmix

The emission spectra of mtagBFP tagged to peroxisome, and mTFP1 tagged to vacuole were plotted in Figure 5-A. The emission spectra of tdTomato tagged to mitochondrion and mCherry tagged to lipid droplets were plotted in Figure 5-B. The emission spectra from the experiments showed clear separations from the other fluorescent proteins, and good agreements with the benchmark spectra used to unmix the spectra. The detailed difference between the benchmark and the bulk experiment spectra should result from the colocalization of the corresponding organelles.

In the preliminary experiments, the fluorescent proteins tagged to endoplasm reticulum (superfolderGFP) and Golgi apparatus (yemCitrine) showed well separated emission spectra under corresponding excitation lasers. (Figure 5-C, Figure 5-D) Therefore, we used non-spectral confocal microscopy in the perturbation experiments to image these organelles to shorten the acquisition time.

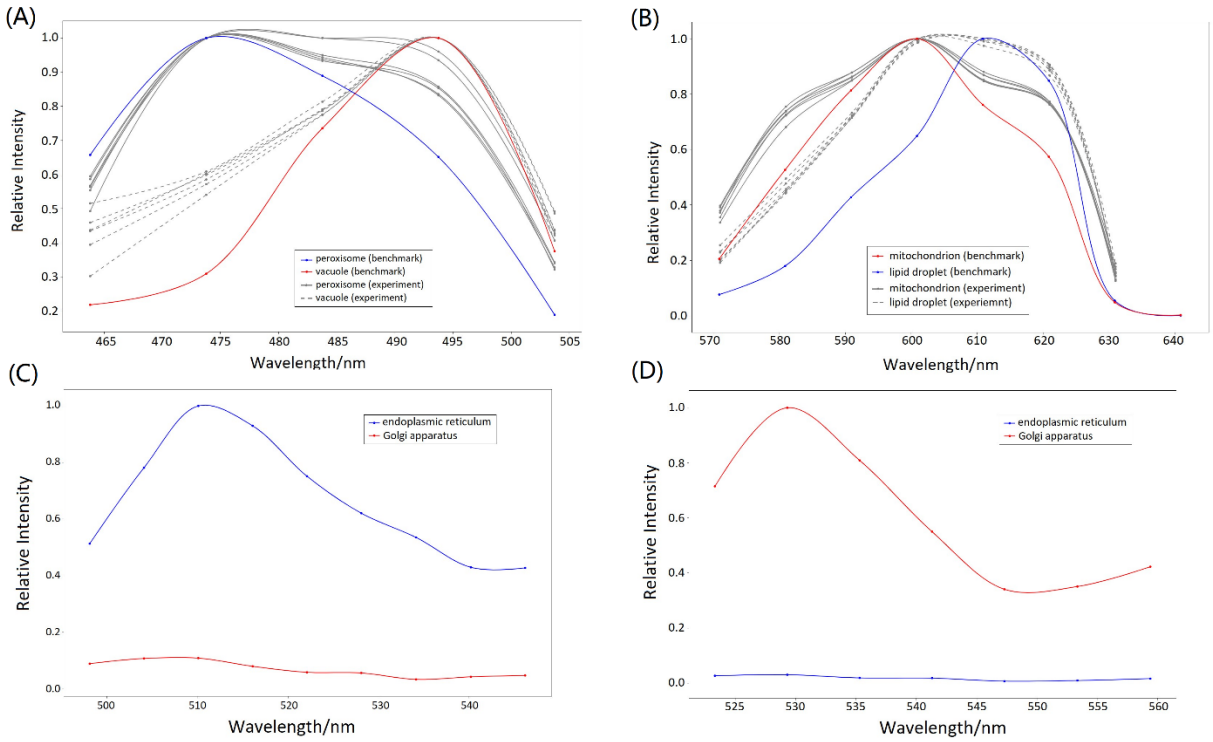

Figure 5 Separation of the emission spectra of the fluorescent proteins under corresponding optical configurations in table 2.

In **(A)** peroxisome (mtagBFP) and vacuole (mTFP1), **(B)** mitochondrion (tdTomato) and lipid droplets (mCherry), the colored lines are benchmark spectra used to unmix the spectral microscopy images. The gray lines are the averaged emission spectra in each perturbation experiment. **(C,D)** endoplasm reticulum (superfolderGFP, blue line) and Golgi apparatus (yemCitrine, red line) were shown to have more separated emission spectra given corresponding excitation laser in the preliminary experiment.

2.3.2 Error Analysis on Image Segmentation

By utilizing the pixel-level posterior probabilities, which determine the likelihood of assigning a specific pixel to a particular organelle type, we were able to estimate the errors associated with our volume fraction measurements. Based on our analysis, we found that the range of errors in these measurements falls between 5% and 10% (Figure 6).

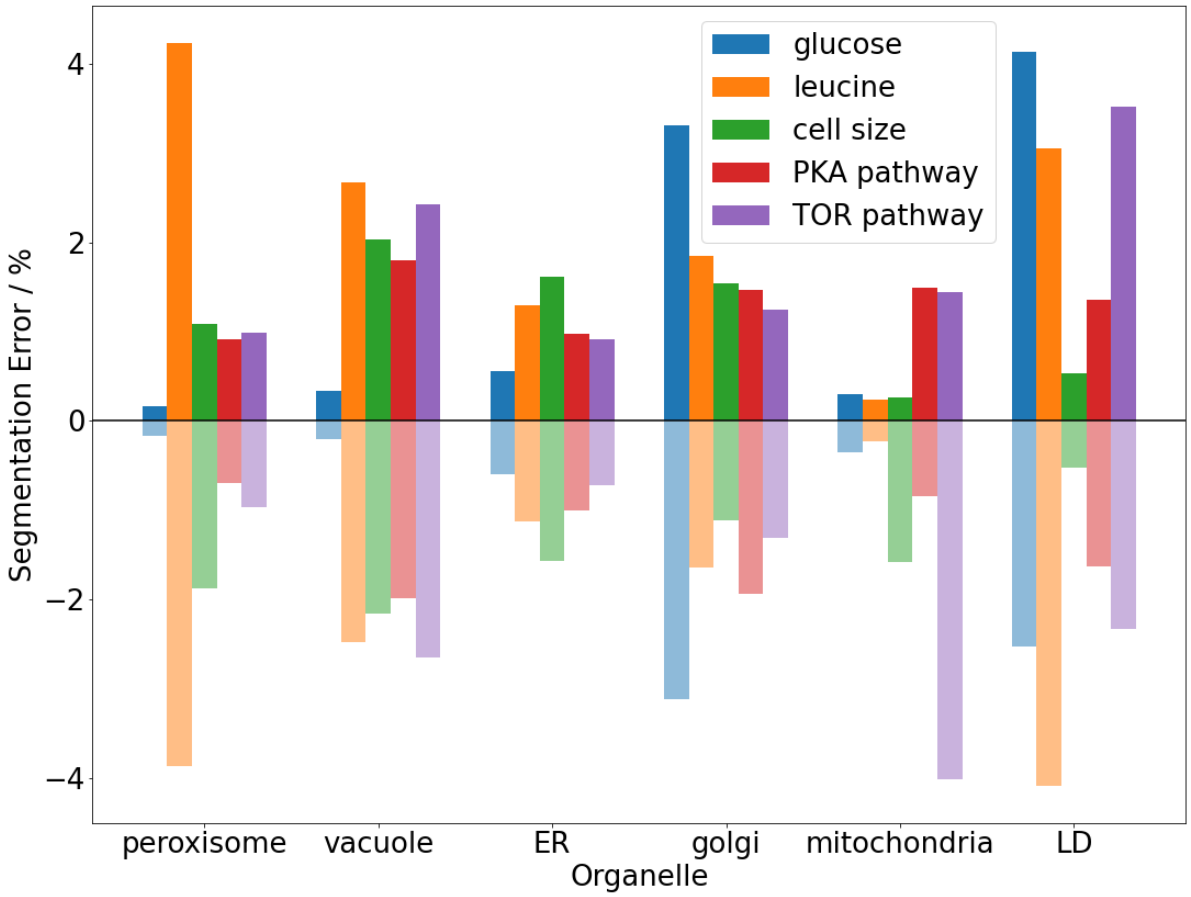

Figure 6 The estimated error of the total volume of 6 organelles across different perturbation experiments.

2.3.3 Cellular Growth Rate and Organelle Property Data

Experiment	Base Medium	Change/Addition	Condition	Alias Name	N (cells)	Growth rate (hr^{-1})
glucose	YNB+CSM	glucose	0	glu-0	1520	0.010
			0.01% m/v	glu-0-5	868	0.147
			0.1% m/v	glu-5	1191	0.310
			1% m/v	glu-50	555	0.461
			2% m/v	glu-100	861	0.427

			4% m/v	glu-200	790	0.480
leucine	SD-leucine	leucine	0	leu-0	1012	0.101
			25 mg/L	leu-25	736	0.166
			50 mg/L	leu-50	1666	0.224
			75 mg/L	leu-75	1080	0.435
			100 mg/L	leu-100	1505	0.516
cell size	SD complete	Whi5 overexpression beta-estradiol	0	Whi5Up-0	651	n/a
			10 µM	Whi5Up-10	353	n/a
PKA pathway	SD complete	1-nm-pp1	0	1nmpp1-0	1640	0.515
			500 nM	1nmpp1-500	1554	0.436
			1.5 µM	1nmpp1-1000	1173	0.396
			3 µM	1nmpp1-3000	1682	0.101
TOR pathway	SD complete	rapamycin	0	rpmc-0	1278	0.509
			100 ng/mL	rpmc-100	1297	0.430
			200 ng/mL	rpmc-200	772	0.421
			400 ng/mL	rpmc-400	1760	0.207
			1000 ng/mL	rpmc-1000	1963	0.201

Table 3 Summary of the perturbation experiments, including the base media, the perturbed biochemical processes, the number of cells in each condition group, and the growth rate measured by OD (600nm)

2.3.4 Correlation Coefficient between Organelle Properties

To validate our data, we performed an analysis utilizing a pairwise correlation coefficient matrix encompassing various properties of the organelles under investigation. Furthermore, we meticulously compared the entries within this matrix with findings from prior studies, as illustrated in Figure 7. In every instance we explored, we observed a notable concurrence

between the outcomes obtained from our comprehensive organelle imaging at the systems level and the previously reported results. For instance, when investigating the association between the overall size of the organelles and the dimensions of their respective host cells, we successfully replicated the positive correlation previously documented for the endoplasmic reticulum (ER), vacuole/lysosome, and mitochondria (Figure 7).

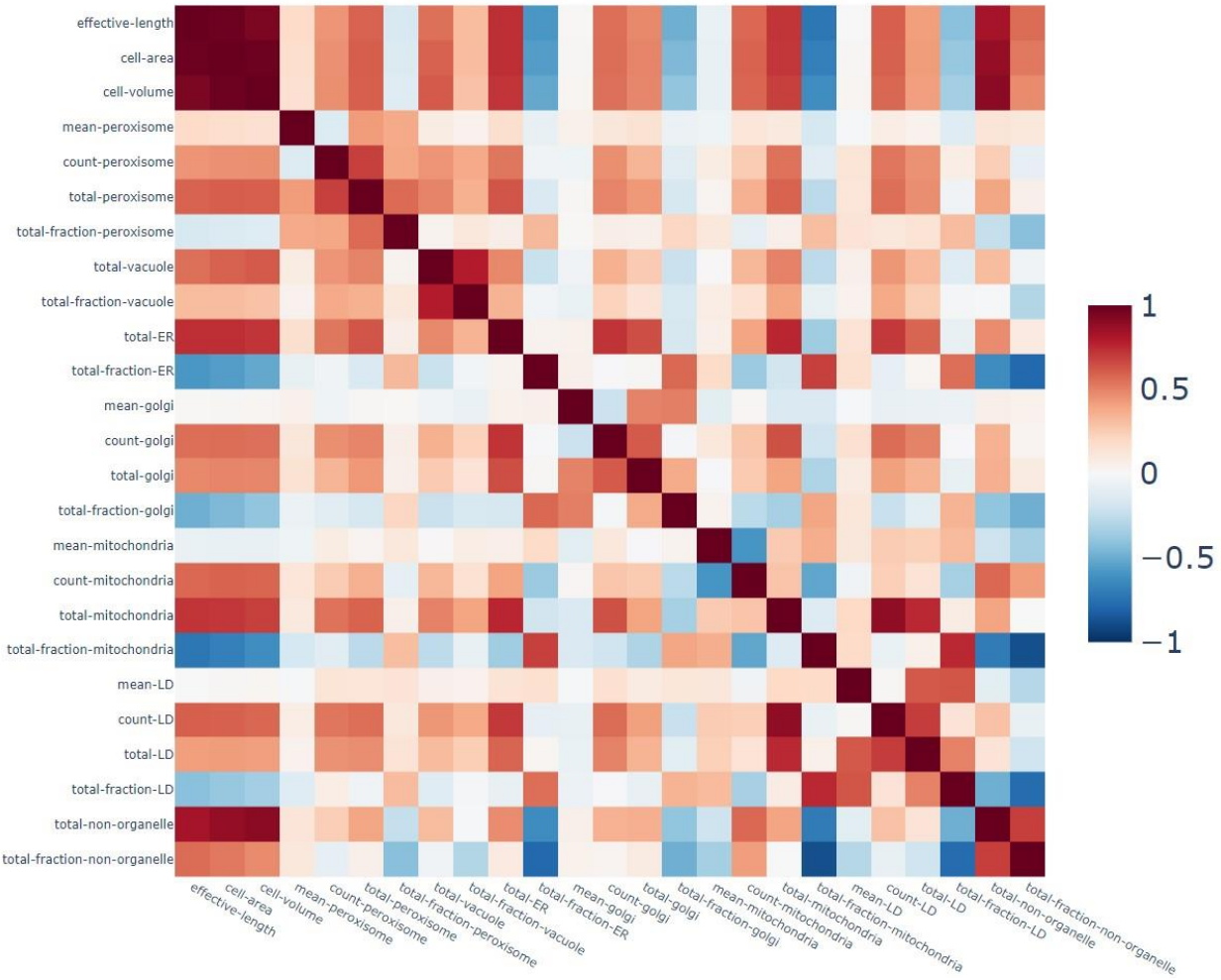

Figure 7 Heatmap depicting the correlation coefficients between organelle properties and cellular characteristics for each individual cell in the **glucose** perturbation experiments.

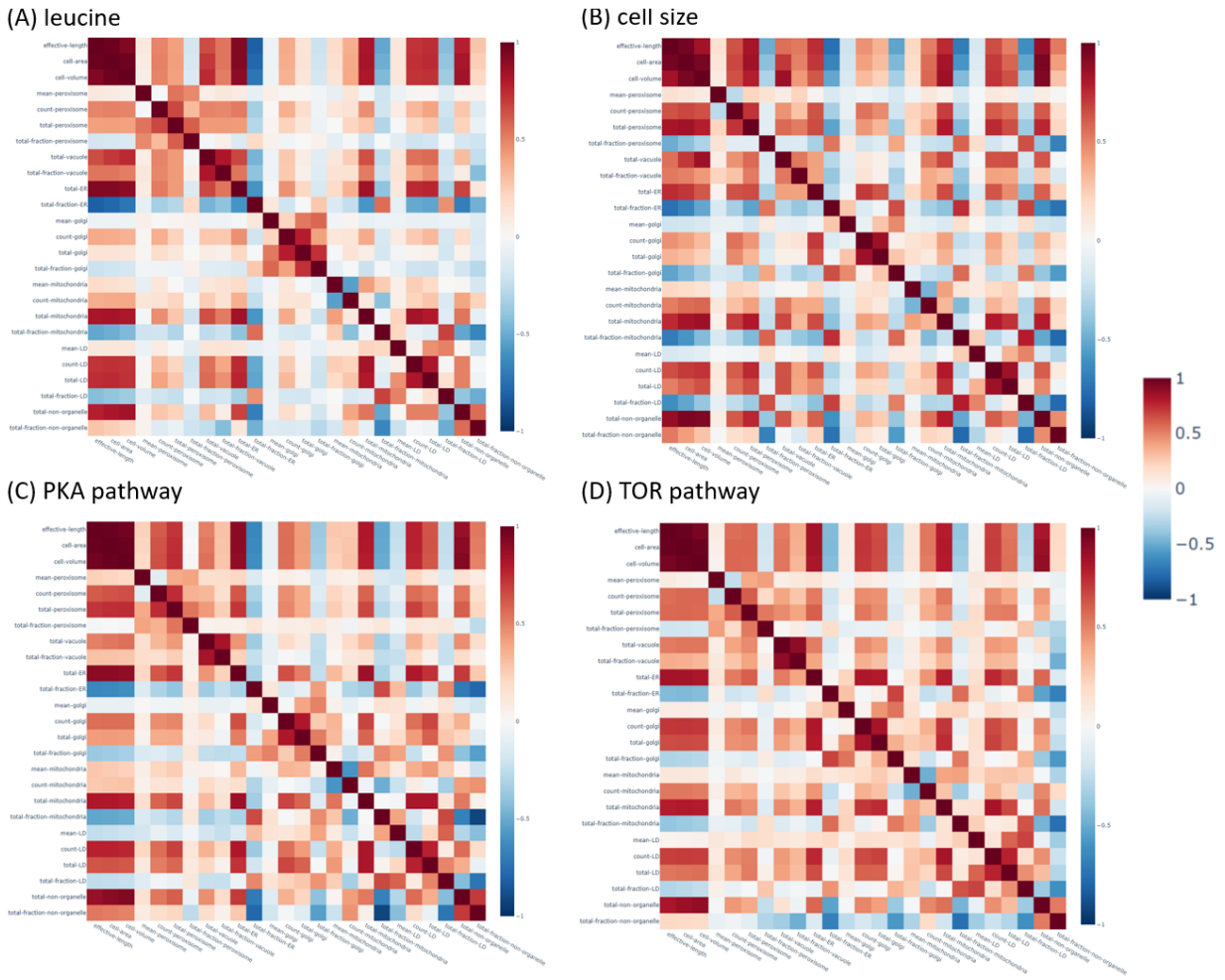

Figure 8 Heatmap depicting the correlation coefficients between organelle properties and cellular characteristics for each individual cell upon different perturbation experiments. **(A)** leucine **(B)** cell size **(C)** PKA pathway **(D)** TOR pathway.

2.3.5 Power Law between Organelle Volume Fractions

Armed with a validated dataset, our primary objective was to differentiate among several models that strive to comprehend the primary limitations imposed by cellular compartments on cell size and growth. For this purpose, we derived volume scaling exponents for each combination of structures we examined, in addition to the cell's volume and an approximation of the nucleocytoplasmic volume (Figure 10).

Certain exponents exhibited congruity with established cell biological associations, notably the positive scaling observed between endomembrane organelles such as the Golgi, peroxisome, and lipid droplet, in relation to the endoplasmic reticulum (ER).

Nonetheless, our comprehension of the role organelle allocation plays in governing cell growth was confronted by two specific sets of exponents. Firstly, the scaling exponents pertaining to the vacuole indicated a disconnection between vacuole biogenesis and the other organelles under investigation. Secondly, the exponents that linked the volume of the cell to the volume of the vacuole and nucleocytoplasm presented further challenges, suggesting intricate relationships yet to be fully elucidated.

Theoretical predictions of the scaling exponent exhibit disagreements based on the proposed mechanisms for limiting cell size. When cell size is limited by bulk protein synthesis, scaling exponents of 1 are favored. Conversely, when cell size regulation is influenced by transport limitations, scaling exponents of 2/3 are favored (Figure 9).

In our study, we made observations within different glucose environments. We found that the volume of the cell obeyed scaling exponents of 0.24 ± 0.01 and 0.60 ± 0.01 for the vacuole and nucleocytoplasm, respectively (see Figure 10). And similar relationships can be observed in other perturbation experiments.

Considering the strong correlation between cell size and growth rate, the sublinear scaling exponent predicts that the volume fraction of the cell allocated to vacuole and nucleocytoplasm should increase as the growth rate increases. This is indeed observed for the nucleocytoplasm, as shown in Fig. 1f. The relationship between increasing nucleocytoplasmic volume fraction and growth rate resembles the "growth law" observed in prokaryotes, leading us to hypothesize that growth is limited by nucleocytoplasmic availability.

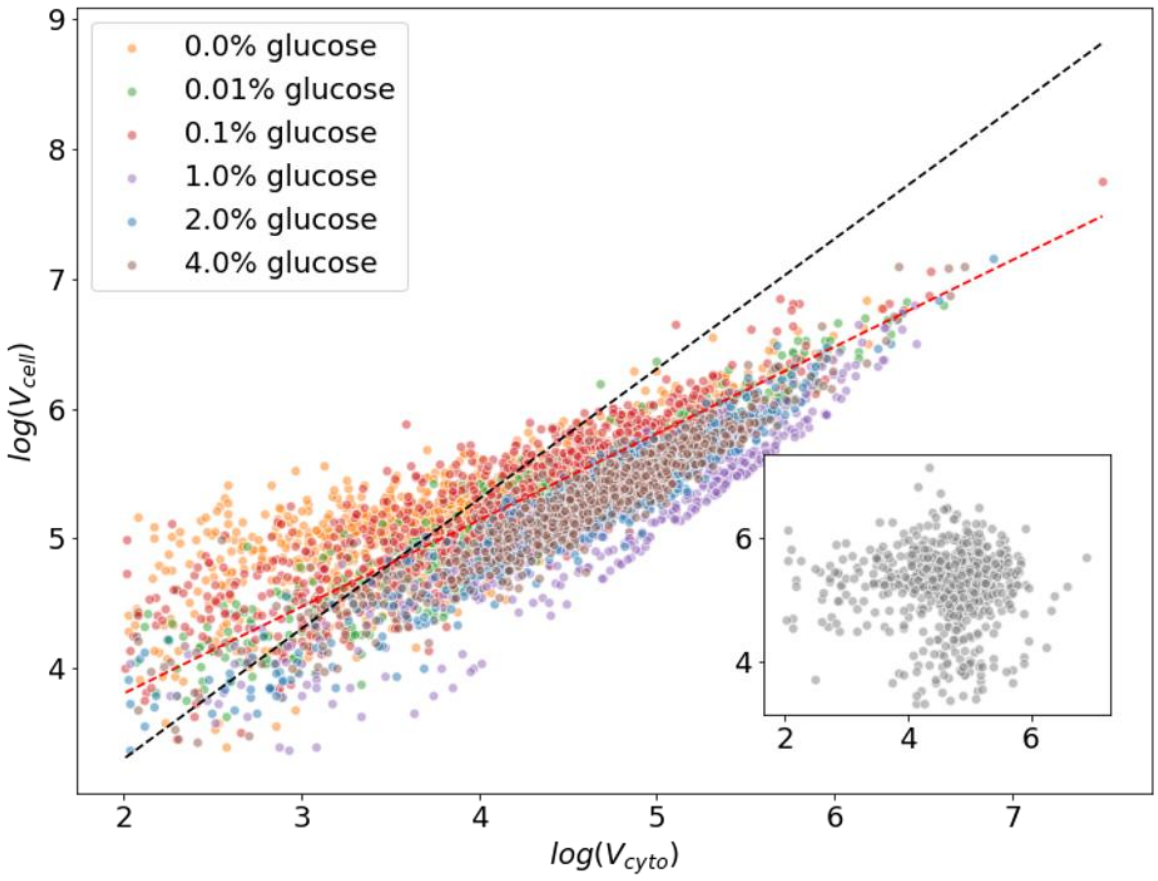

Figure 9 Log-log relationship between the volumes of the cells and the cytoplasm. The inlet is the benchmark shuffled from the data in the 2.0% glucose experiment. The black line is the exponent 1 line, while the red line is the linear regression form the log-log data.

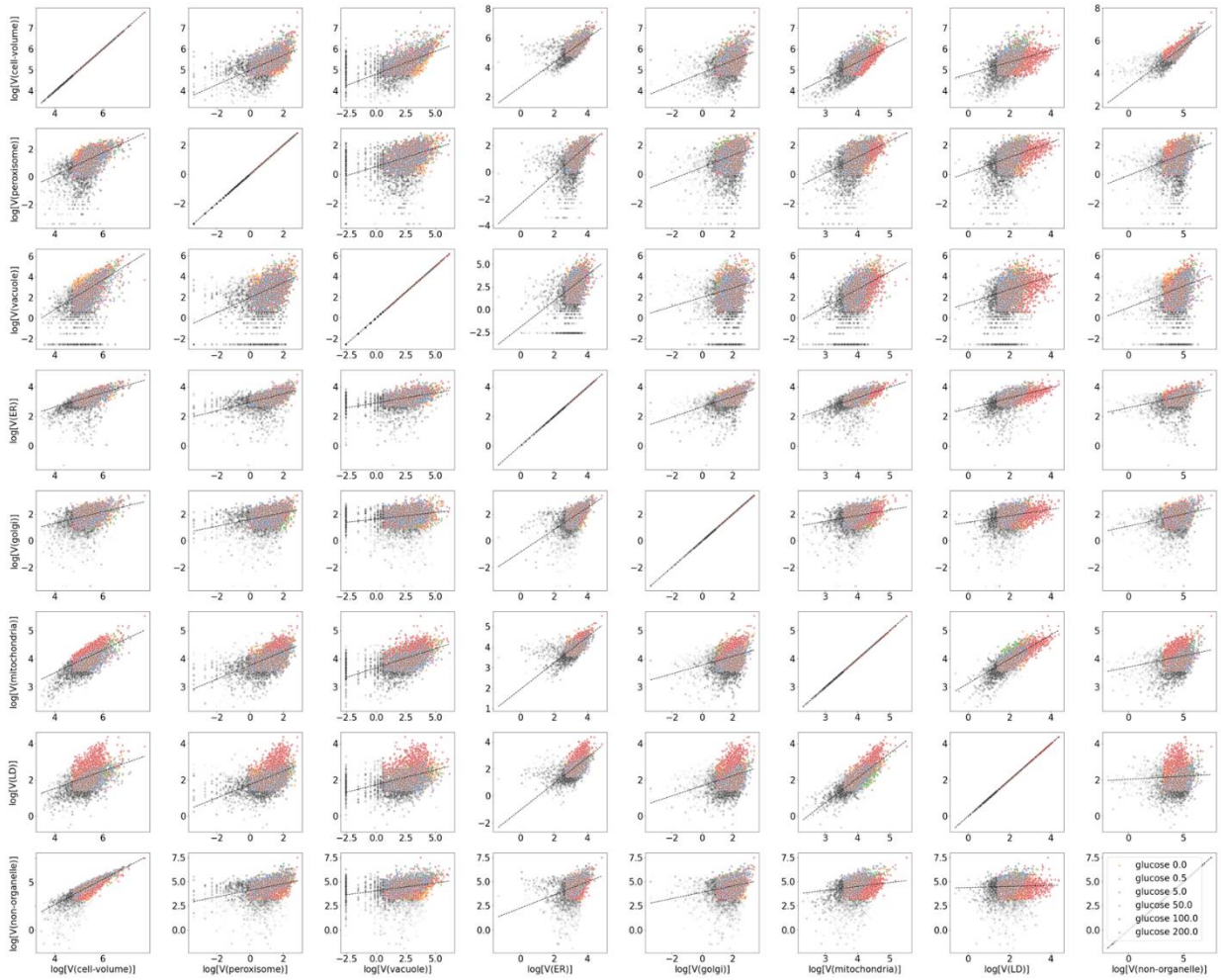

Figure 10 Log-log plots of total volumes of 6 organelles, total volume of the cell, and estimate of nucleocytoplasmic volume in the **glucose** perturbation experiments

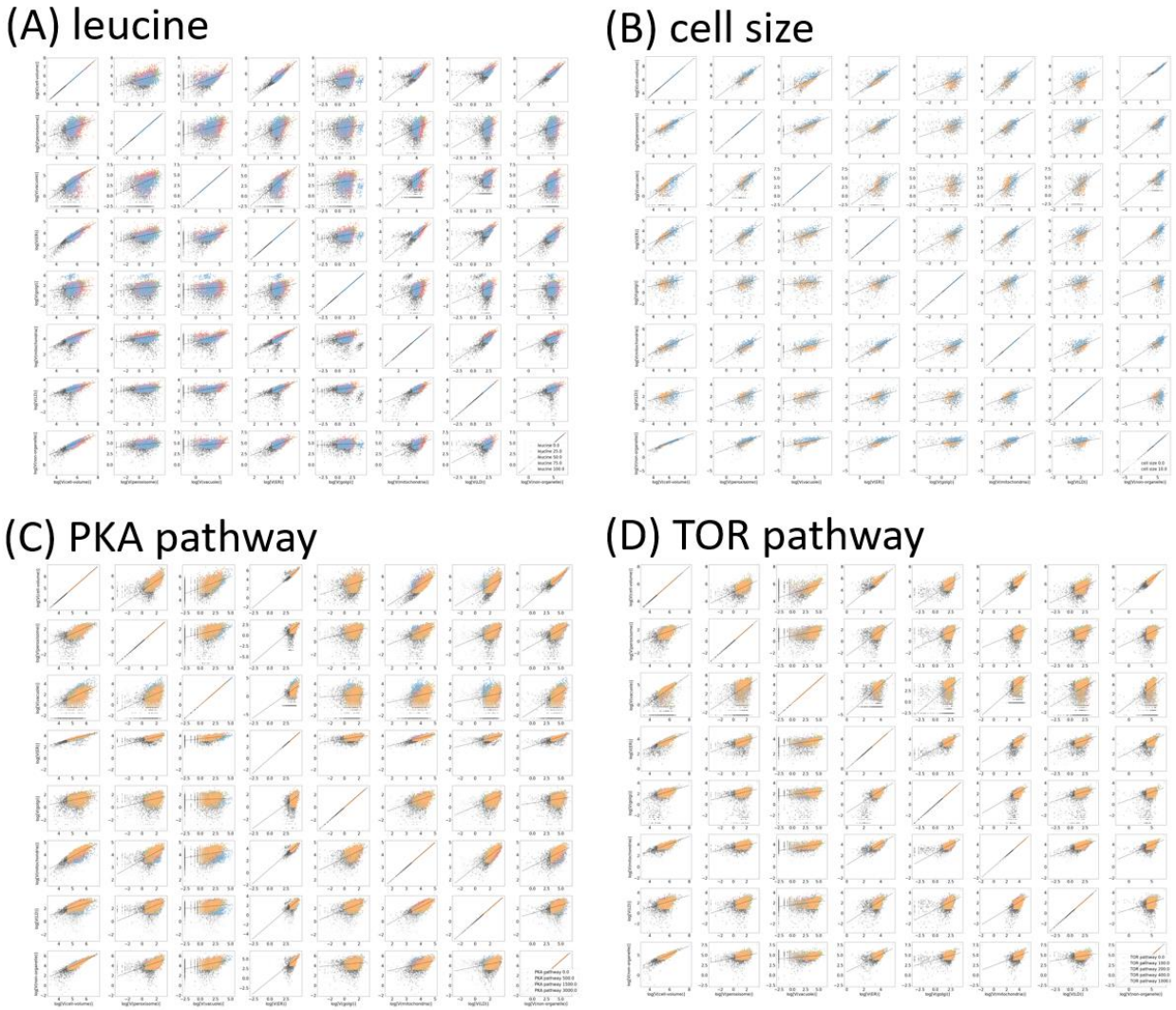

Figure 11 Log-log plots of total volumes of 6 organelles, total volume of the cell, and estimate of nucleocytoplasmic volume from different perturbation experiments: **(A)** leucine **(B)** cell size **(C)** PKA pathway **(D)** TOR pathway. Lines are the linear regression within each condition.

However, we encountered a contradiction when examining the vacuole. To investigate further, we measured how organelle allocations are adjusted in various growth contexts to match the supply of each compartment with the demands of growth.

2.3.6 Entropy and Mutual Information between Cellular Growth Rate and Organelle Properties

In order to assess the degree of organization in the process of organelle biogenesis at the systems level, we conducted an analysis to examine the consistency of changes in organelle profiles when exposed to variations in glucose concentration. To gain insights into how cells distribute their limited resources and energy, our investigation primarily focused on the fractions of organelle volumes.

To quantify the magnitude of change, we employed the Kullback-Leibler divergence [29] to compare the distributions of organelle volume fractions among cell populations cultivated under different glucose concentrations. Specifically, we utilized 2% glucose as the reference concentration against which measurements were taken. To evaluate the coherence of any observed changes, we calculated the Shannon entropy of the organelle volume fraction distributions for each population. By comparing the relative changes in Shannon entropy and KL divergence as cells were subjected to varying glucose concentrations, we made the noteworthy observation that the KL divergence exhibited an increase of 200-400% compared to the reference population. This indicates that cells do indeed modify their allocation of organelles in response to fluctuations in glucose. In contrast, the Shannon entropy only experienced a 10% change (Figure 12), suggesting that the organelle profiles of cells remain comparably constrained under both low and high glucose levels.

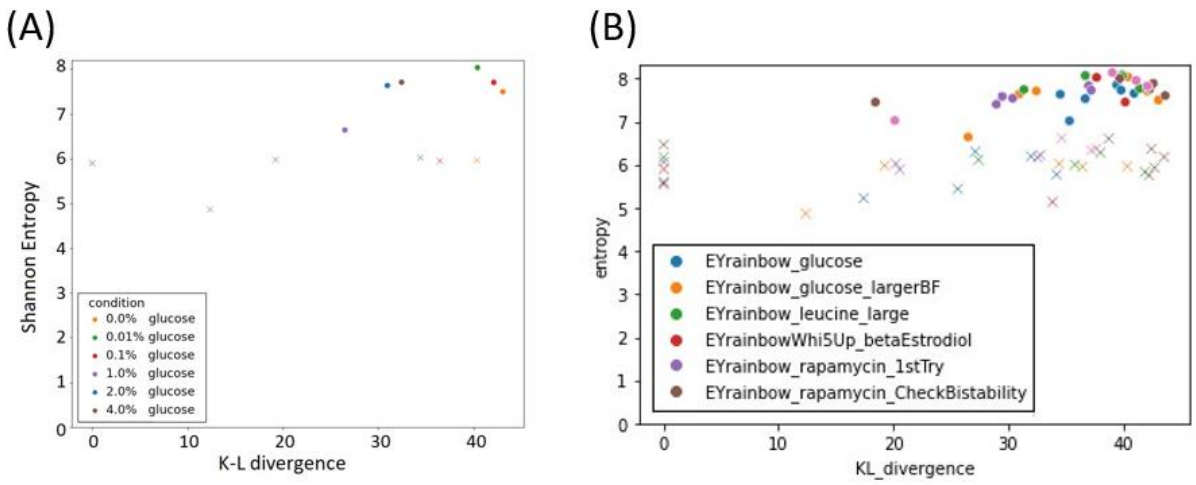

Figure 12 Comparison of Shannon entropy and Kullback-Leibler divergence of the organelle volume fraction distribution **(A)** under different glucose concentrations with respect to 2% glucose (B)

2.3.7 Principal Component Analysis on Organelle Volume Fractions

Based on our information theoretic analysis, which indicated that cells exhibit a relatively consistent pattern of changes in organelle volume fractions, our objective was to identify these changes. To accomplish this, we employed hyperspectral imaging of rainbow yeast and subjected the obtained results to principal components analysis. From this analysis, we computed a vector referred to as the "condition vector," connecting the centroids of the data from each experimental condition (Figure 4). Upon examining the first three principal components, we observed a significant correlation between the position of an individual cell in this space and the glucose environment in which it was cultured (Figure 13-A).

In order to gain a deeper understanding of the cell biology implications inherent in the data's structure along its principal components, we represented the principal components in terms of the

changes in organelle volume fractions along these components (Figure 13-B). Furthermore, we evaluated the degree of co-linearity between these principal components and the condition vector, averaged across multiple glucose conditions. When expressed in this manner, the first principal component revealed a decrease in volume fractions for all organelles except the vacuole with increasing glucose concentration in the environment (Figure 13-B). The second principal component demonstrated a decrease in vacuole volume fraction. As for the third principal component, it primarily exhibited a combination of decreasing mitochondrial and lipid droplet volume fractions alongside increasing peroxisomal and Golgi volume fractions (Figure 13-B).

Rather than acting in isolation, our systems-level perspective uncovered patterns of interconnected organelle biogenesis in response to glucose availability. Notably, our data-driven identification of organelle changes, which was independent of the glucose environment in which the cells were cultured, aligns with previous findings in yeast physiology. For instance, earlier studies have shown that decreasing glucose concentrations lead to a shift towards respiration over fermentation and reduced membrane demand due to diminished growth. This concurs with our observed coupling of upregulated mitochondrial and lipid droplet volume fractions with downregulated peroxisome and Golgi volume fractions upon decreasing glucose levels (Figure 13).

The limitation of nutrients, as observed in natural settings, such as glucose scarcity, typically leads to reductions in both cell size and growth rate. [30, 31, 32, 33, 34, 35, 36, 37] This

correlation poses a challenge to identifying the specific physiological signals driving the observed patterns of organelle biogenesis. Therefore, our objective was to distinguish how cell size and growth rate can independently activate the identified organelle modes. To investigate these possibilities, we conducted two additional analyses on our rainbow yeast cells.

To examine the effects of nutrient-independent cell size control, we introduced a plasmid containing a copy of the Whi5 gene under the control of an inducible promoter responsive to beta-estradiol [38, 39]. Although the exact mechanism by which Whi5 expression levels alter cell size is still under investigation, our experiments revealed an approximate 2.4-fold increase in cell size upon exposure to saturating levels of -estradiol.

To investigate the effects of non-natural growth rate dependence, we took advantage of the fact that rainbow yeast cells were genetically modified to be auxotrophic for the amino acid leucine. This artificial leucine autotrophy disrupts the natural connection between cell size and growth rate (Figure 14). By modulating the levels of leucine in the growth medium, we were able to manipulate the growth rate accordingly [40]. Subsequently, we conducted hyperspectral imaging on rainbow yeast cells cultivated under various concentrations of leucine and -estradiol in the culture medium.

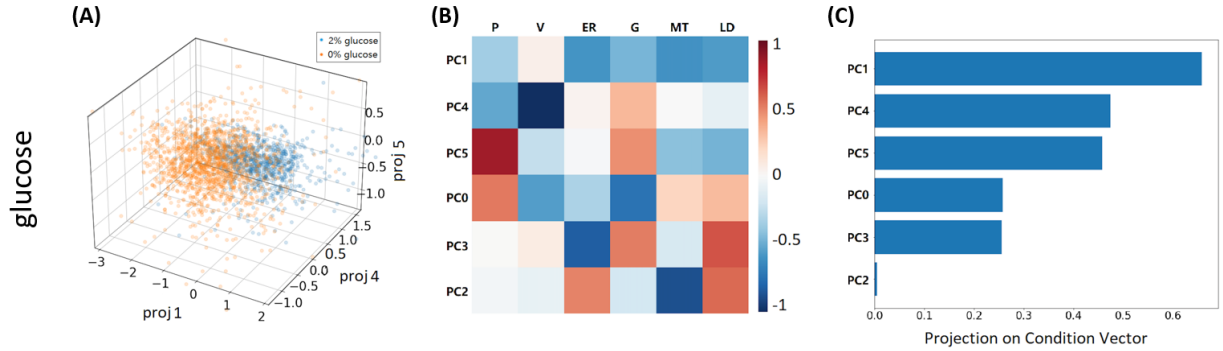

Figure 13 The principal component analysis result on the normalized organelle volume fractions in the **glucose** perturbation experiment. **(A)** The projection of organelle volume fraction data onto 3 principal components that are most aligned with the condition vector. **(B)** Heatmap of the principal components of normalized organelle volume fractions and their corresponding constituent organelles. **(C)** The cosine of the angle between the condition vector and various principal components, sorted in descending order.

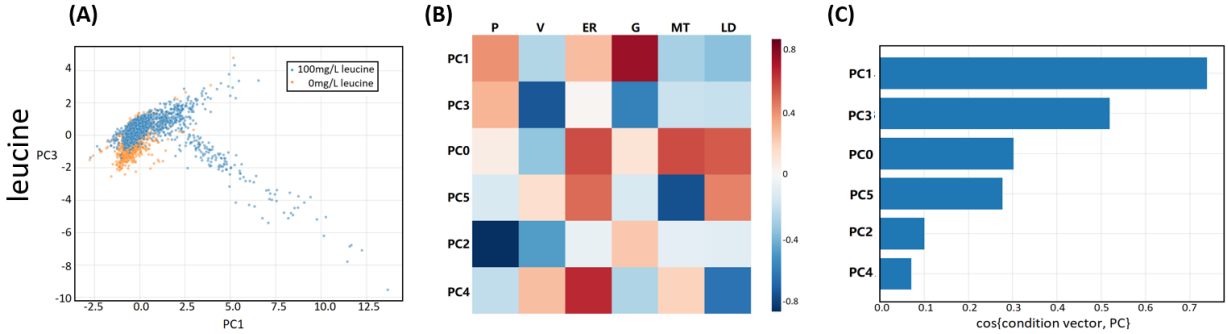

Figure 14 The principal component analysis result on the normalized organelle volume fractions in the **leucine** perturbation experiment. **(A)** The projection of organelle volume fraction data onto 2 principal components that are most aligned with the condition vector. **(B)** Heatmap of the principal components of normalized organelle volume fractions and their corresponding constituent organelles. **(C)** The cosine of the angle between the condition vector and various principal components, sorted in descending order.

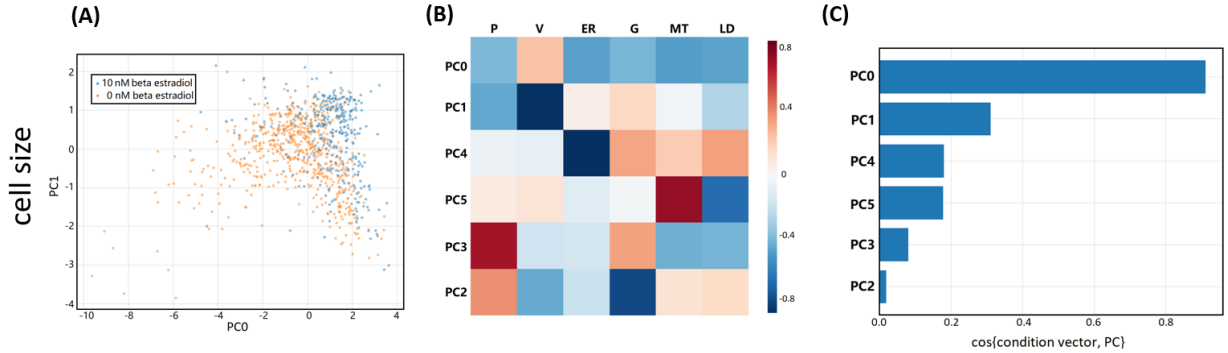

Figure 15 The principal component analysis result on the normalized organelle volume fractions in the **cell size** perturbation experiment. **(A)** The projection of organelle volume fraction data onto 2 principal components that are

most aligned with the condition vector. **(B)** Heatmap of the principal components of normalized organelle volume fractions and their corresponding constituent organelles. **(C)** The cosine of the angle between the condition vector and various principal components, sorted in descending order.

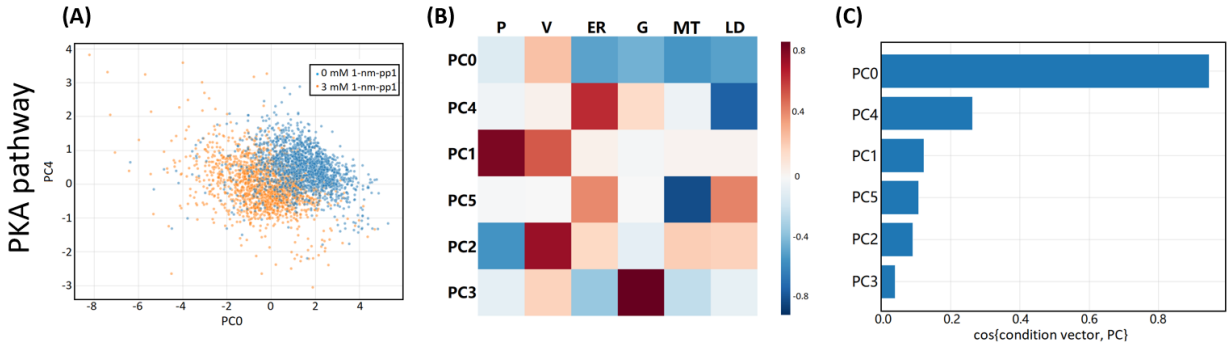

Figure 16 The principal component analysis result on the normalized organelle volume fractions in the **PKA pathway** perturbation experiment. **(A)** The projection of organelle volume fraction data onto 2 principal components that are most aligned with the condition vector. **(B)** Heatmap of the principal components of normalized organelle volume fractions and their corresponding constituent organelles. **(C)** The cosine of the angle between the condition vector and various principal components, sorted in descending order.

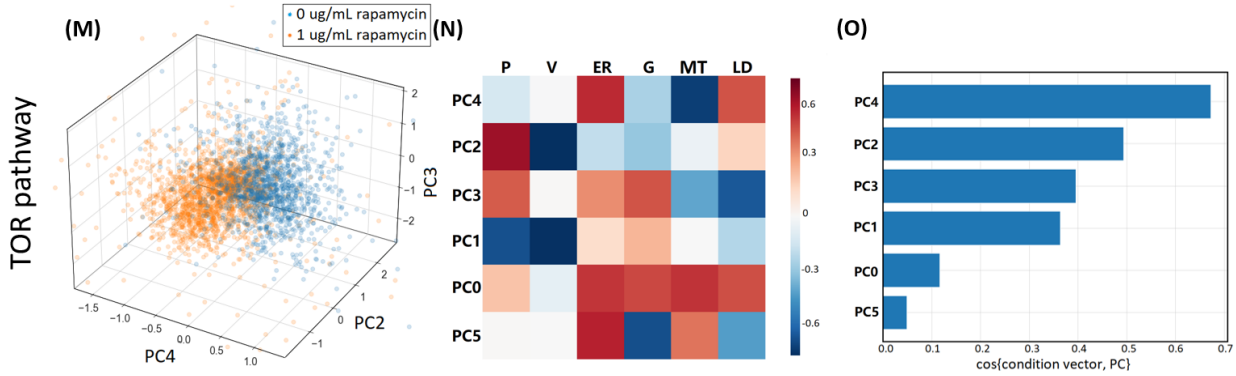

Figure 17 The principal component analysis result on the normalized organelle volume fractions in the **TOR pathway** perturbation experiment. **(A)** The projection of organelle volume fraction data onto 3 principal components that are most aligned with the condition vector. **(B)** Heatmap of the principal components of normalized organelle volume fractions and their corresponding constituent organelles. **(C)** The cosine of the angle between the condition vector and various principal components, sorted in descending order.

2.3.8 Condition Vectors and theirs Projections in PCA Space

To gain a mechanistic understanding of whether the observed patterns of systems-level organelle biogenesis are driven by physical constraints arising from cell size and nutrient availability, or if

they can be provoked solely by information from growth-regulating signaling pathways, we employed chemical biology tools to manipulate growth signaling. In budding yeast, the two major growth signaling pathways are the target-of-rapamycin (TOR) and protein kinase A (PKA) pathways [41, 42]. Our aim was to characterize the systems-level organelle biogenesis profile in terms of organelle fractions, as influenced by TOR activity (specifically TORC1) and PKA signaling strengths.

For the TOR pathway, we utilized the small molecule inhibitor rapamycin to modulate TORC1 activity. In the case of the PKA pathway, we engineered rainbow yeast with mutations in the PKA pathway genes TPK1, TPK2, and TPK3, rendering these enzymes responsive to inhibition by the small molecule 1-nm-pp1 [8, 43]. We then exposed rainbow yeast to varying concentrations of rapamycin and 1-nm-pp1, conducted hyperspectral imaging, and plotted the principal components in the space defined by organelle volume fractions (Figure 16, Figure 17) [11].

Our observations indicate that the first principal component, associated with TOR signaling, closely aligns with the organelle modes responsive to leucine deprivation (Figure 14-B, Figure 17-B). This finding is consistent with TOR signaling being sensitive to leucine levels [43]. On the other hand, the organelle mode primarily influenced by PKA pathway activity (Figure 15-B) demonstrates a significant co-linearity with the mode responsive to cell size (Figure 16-B). These results suggest that TOR and PKA signaling pathways establish connections between cell growth rate and cell size, respectively, and systems-level organelle biogenesis [11].

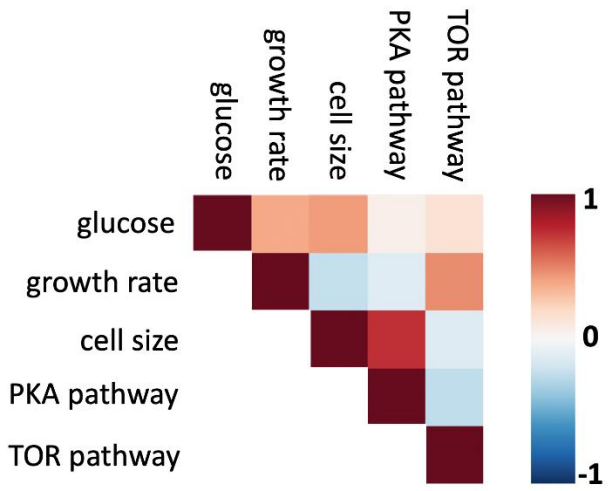

Figure 18 The similarities of condition vectors' projection onto principal components between each pair of experiments

2.4 Discussions

The organelles within cells exhibit a fascinating combination of interactivity and modularity. Their intricate structure and functions pose a significant challenge in comprehending the fundamental principles that govern their biogenesis. By employing a top-down, data-driven approach, we shed light on the underlying mechanisms that regulate organelle biogenesis in response to physiological cues. This novel perspective allows us to delve deeper into the intricate connections established among organelles, despite the intricate and multiscale processes that govern their formation and functionality. Through this comprehensive approach, we unraveled the mechanisms that orchestrate the intricate dance of organelles within the cellular environment.

Our research endeavors have involved meticulous analysis of the pairwise correlations between organelle volume fractions and the size of host cells, yielding intriguing findings. Remarkably, our data reveals a compelling inverse correlation between the volume fractions of organelles and

the size of the host cell. In other words, as cells grow larger, organelles occupy a relatively smaller fraction of the cellular space. This observation has led us to delve deeper into the growth patterns of organelles, particularly focusing on size scaling exponents below 1. By investigating these patterns, we have uncovered a fascinating phenomenon. It appears that by promoting the growth of organelles with size scaling exponents less than 1, a greater proportion of the cell can be allocated to nucleocytoplasm, which in turn facilitates increased organelle volumes required to accommodate the rapid growth observed in certain cellular contexts [11].

In addition to uncovering the intriguing dynamics of organelle biogenesis, our research has shed light on the intricate coordination between system-level organelle growth and the host cell itself. Contrary to the prevailing notion of fixed fraction allocation, our data suggests that the growth rates of both organelles and the host cell are closely intertwined. This coordination ensures that the biogenesis of organelles occurs in harmony with the overall growth of the cell, thereby fostering efficient cellular functioning. By establishing a delicate balance between organelle growth rates and the host cell's development, the cellular environment maintains a robust and optimized state conducive to the demands of various physiological processes [11].

One of the crucial insights arising from our research is the mechanistic role played by PKA and TOR signaling activity in linking the growth rate and cell size to the process of organelle biogenesis. This significant conclusion would have been elusive without adopting a systems-level perspective. Our measurement strategy, designed to effectively capture the intricate dynamics of systems-level organelle biogenesis, possesses a remarkable degree of

generalizability. It can be readily applied to investigate the impact of disruptions in the organelle contact network on organelle biogenesis under diverse physiological conditions. For instance, our approach holds promise in unraveling the intricate dynamics of organelle biogenesis in aging cells or within the complex multicellular tissues. In such contexts, organelle biogenesis must simultaneously fulfill the universal cell biological requirements and the unique metabolic demands specific to each cell type. By adopting our comprehensive measurement strategy, researchers can gain valuable insights into the intricate interplay between organelle biogenesis and the diverse physiological states encountered in complex biological systems [11].

Chapter 3: Quantitative Model of Organelle Resource Allocation and Experimental Validation with Biomolecular Condensate

3.1 Introduction

Given the system-level experimental observations and the phenomenological analysis of organelle biogenesis data, we seek to deepen our understanding of how cells distribute resources among organelles to achieve growth goals with quantitative models. Specifically, we would like to explain the seemingly contradictive observations in our previous experiments. The system organelle experiments showed this allocation process is influenced by specific signals derived from the sensed size and growth rate of the cell, which are indicated by the activity levels of the PKA and TOR signaling pathways. However, the increase in TOR and PKA signaling, both of which are associated with cell size enhancement in response to natural stimuli, leads to opposite effects on the volume fraction of the cell occupied by the vacuole [11].

In our model, the cell detects variations in cell volume, and assigns volumes beyond necessary to vacuoles, to maintain the nucleocytoplasmic volume fraction. This principle in the design directly results in a consistent nucleocytoplasmic volume fraction, while the volume fractions of other organelles decrease as the cell expands in constant growth conditions. To verify this hypothesis, we utilized a newly engineered synthetic biological condensate called PopTag, derived from Caulobacter crescentus. The PopTag was employed to artificially increase the crowding effect within the cytoplasm. The outcome aligns with our proposed concept that the cell separates the responsiveness of organelle modes to cell size and growth rate [12].

3.2 Methods

3.2.1 Mathematical model of organelle resource allocation

When there is a fluctuation in cell volume V_{cell}, the cell could allocate the fluctuation δV to either the cytoplasm, or maintain the volume fraction of cytoplasm and send the extra volume to vacuoles.

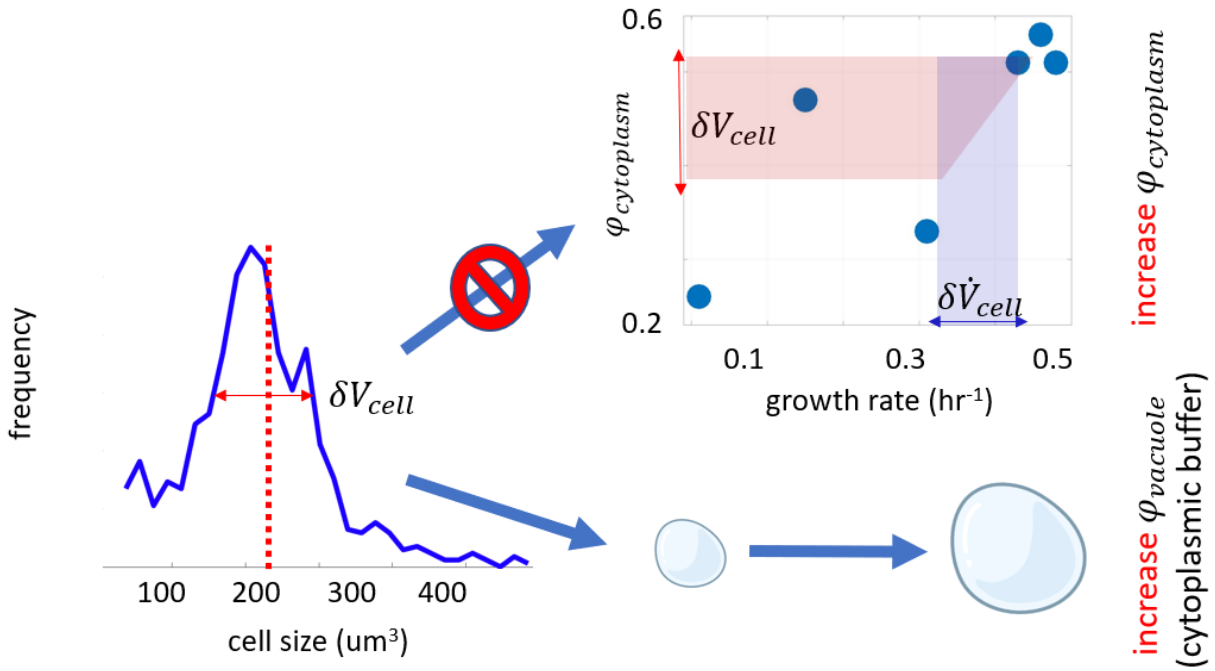

Figure 19 illustration of organelle allocation model, which utilizes the architecture of organelle modes to enable fluctuations in cell size to be absorbed by corresponding fluctuations in vacuole size.

Volume fluctuation allocated to cytoplasm

The volume fraction of cytoplasm will be modified:

$$\phi_{cyto} = \frac{V_{cyto}}{V_{cell}} \rightarrow \frac{V_{cyto} + \delta V}{V_{cell} + \delta V}$$

Taylor expand and neglect the terms higher than the second order:

$$\begin{aligned} \phi_{cyto} &= \frac{1}{V_{cell}} \frac{V_{cyto} + \delta V}{1 + \frac{\delta V}{V_{cell}}} \\ &\approx \frac{1}{V_{cell}} (V_{cyto} + \delta V)(1 - \frac{\delta V}{V_{cell}}) \\ &\approx \phi_{cyto} + (1 - \phi_{cyto}) \frac{\delta V}{V_{cell}} \end{aligned}$$

The second term means the fluctuation of cell volume could result in an increase in nucleocytoplasmic volume fraction, even in the constant growth phase. As a consequence, there could be a discrepancy between the supply of nucleocytoplasmic volume fraction and the demands of growth.

Volume fluctuation maintains cytoplasm fraction, with extra volume allocated to vacuoles

$$\phi_{vac} - \phi_0 = \left(1 - \phi_{cyto}\right)\frac{\delta V}{V_{cell}}$$

where ϕ_0 is the minimum apparent vacuole size.

$$\phi_{vac} - \phi_0 = (1 - \alpha\lambda)\frac{\delta V}{V_{cell}}$$

The volume fraction of cytoplasm ϕ_{cyto} is linearly correlated with the growth rate λ:

Upon examining this equation, we observe two important trends. First, we observe a positive correlation between the volume fraction of the vacuole and the variability in cell volume under constant conditions (constant growth rate λ; PKA organelle mode). Second, we observe a decrease in the overall average vacuole volume fraction as the growth rate increases across different conditions (TOR organelle mode).

To generate experimentally verifiable hypothesis from this framework, we consider a situation when introducing a biomolecular condensate. Based on our model, we hypothesized that the presence of the biomolecular condensate would lead to corresponding modifications in the vacuole volume fraction:

$$\phi_{vac} - \phi_0 = (1 - \alpha\lambda)\frac{\delta V}{V_{cell}} - \phi_{condensate}$$

3.2.2 Experiment validation with biomolecular condensates

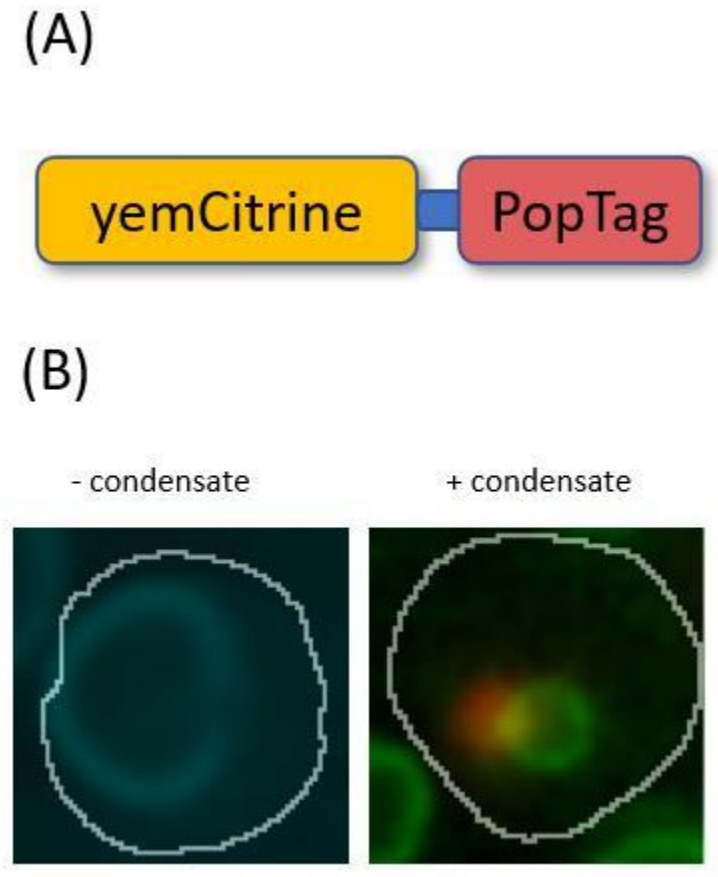

Figure 20 (Left) example image of cells expressing Vph1-mCerulean3 to visualize vacuoles in the absence of PopTag-YFP constituted biomolecular condensates. (Right) example image in the presence of PopTag-YFP constituted biomolecular condensates.

The above model presents a robust prediction: when the nucleocytoplasmic compartment is artificially constrained under constant growth conditions, the vacuole should respond by reducing the extent to which its volume fraction increases with cell size. To verify this prediction, we utilized the PopTag, a synthetic biological condensate derived from Caulobacter crescentus, to induce crowding within the cytoplasm. We attached monomeric Citrine to the C-terminal end of the PopTag and relied on inherent stochastic fluctuations in PopTag expression

(Figure 19-A). This experimental setup allowed us to monitor the response of each organelle to this spatial perturbation (Figure 19- B)

3.3 Results and Discussion

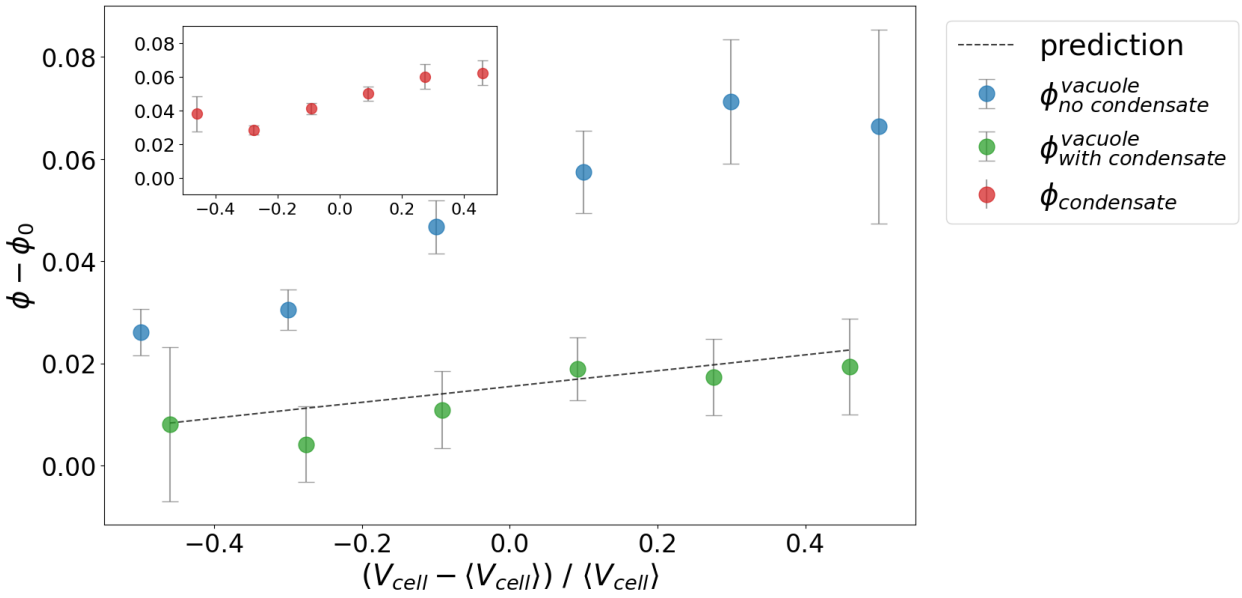

Figure 21 Change in vacuole volume fraction in response to variability in cell volume in the 2% glucose environment. In the absence of the biomolecular condensate (blue dots), the vacuole volume fraction exhibits a certain pattern. However, in the presence of the biomolecular condensate (green dots), the vacuole volume fraction shows a different trend, as illustrated in the inset (red dots). The black dashed line represents the predicted change in the vacuole volume fraction when the biomolecular condensate is present.

Our observations indicate that as cells increase in size, the volume fractions of PopTag-YFP also increase (Figure 20, inset). However, in the same cells, the volume fraction of the vacuole decreases compared to its non-crowded counterpart (Figure 20). Remarkably, our mathematical model enables us to predict the change in the slope that describes the relationship between the vacuole volume fraction and cell size (Figure 20, black dashed line) [41].

This finding supports our concept that the cell separates the responsiveness of organelle modes to cell size and growth rate, allowing the vacuole to play a pivotal role in buffering the cell against fluctuations in cytoplasmic availability. Consequently, the cell can adjust the allocation of compartments to align with its growth environment.

Chapter 4: Organelle Recognition from Bright Field Fluorescent Microscopy Empowered by Deep Learning

4.1 Introduction

In the research covered in the previous chapter, the organelle data were collected 3 hours after the switch of culture from replete media. At that time the cells are in the exponential growth stage, which means their growth rate is steady. The extracted statistics are able to reveal cell's different long-lasting responses to various perturbed environments, in terms of different modes in organelle size and population. However, this cannot capture the dynamic process in which cells switch to new organelle modes when the environment changes. The temporal data of the population and sizes of different organelles in individual cells, could offer hints about the mechanisms cell use to regulate different organelles, in order to achieve their growth goals.

An imaging system maps objects in the physical world into data of the same or lower dimensional image space [44]. An optical imaging system achieves this by collecting the photons emitted from the objects during the imaging time onto a sensor of a limited size [45]. Imaging goals include but are not limited to: high spatial resolution, high spectral color resolution, high temporal frame rate, wide field of view, and low photodamage to samples. Different imaging techniques have different trade-offs between the goals, because of the imperfection of imaging components, limited sensor size, and limited exposure time [44] [45].

An optical microscope is a diffraction-limited system, giving the spatial resolution an upper limit at the order of the wavelength of the emitted photons. Mathematically, the image vector is considered as the convolution between the object and the point spread function (PSF) of the imaging system. The point spread function is measures by taking the image of a single point at the size of the diffraction limit. The intensity of a given pixel in the image is the sum of the diffraction patterns of all points in the object [44].

4.1.1 Confocal Microscopy

Confocal microscopy minimizes the effect of diffraction at the image acquisition stage. It has pinholes on the light path in front of and behind the lens, so that at any time only one point of object is lit up and only photons from that point are collected by the sensor. The point spread function is approximately a unit vector. This method can achieve the spatial resolution near the diffraction limit [46].

The scanning of the pinholes gives confocal microscopy a lower time resolution than traditional microscopy, and requires precise micro-controlling. The high proportion of rejected photons requires a stronger light source, which can be photodamaging to the fluorescent proteins. The optical configuration in the previous chapter suffered from a spatial resolution of 0.4 um in pixel size, and a low frame rate of ~5 minutes per field of view [11].

4.1.2 Spectral Imaging

One defining novelty of the research project in the previous chapter is the simultaneous measurements of several organelles in individual cells. The requires a high spectral resolution to separate the signals from different fluorescent proteins having overlapping emission spectra. This was enabled by a diffraction gating that separates photons of different wavelengths onto a linear multi-anode array detector downstream of the confocal pinhole. The photons of various wavelengths are diffracted at different distances in higher-index diffraction peaks, thus decoding spectral information into spatial information. Counting the number of photons in corresponding sensor channels yields the emission spectra of the sample. Comparison and linear decomposition with the emit spectra of known fluorescent proteins gives the relative intensity of corresponding fluorescent proteins [47].

The disadvantage of this technique is that the number of photons into each spectral channel is reciprocal to the number of channels, leading to a low signal to noise ratio. A higher light source power and longer acquisition time are used to compensate this shortcoming. This further lowers the temporal resolution of the data.

4.1.3 sCMOS Camera

sCMOS (scientific Complementary Metal-Oxide-Semiconductor) is the default alternative to spectral detector in microscopy. It enables low noise, high frame rate, and wide field of view. It allows LCD rather than the high-power laser to be used as the light source, thus avoids

photodamage to the sample and allows timelapse acquisition. [48] In our current hardware setting, the Hamamatsu ORCA-Flash4.0 camera has a frame rate of ~10 frames per second per field of view, and a pixel size down to 0.1 um [11].

However, although the lack of confocal pinhole could increase the light flux and avoid photobleaching, the out-of-focus light blurs the image of the object due to diffraction. Moreover, without the diffraction grating to resolve the wavelength of the emitted photons, the spectral resolution of the system depends on the emission filter. The allowing wavelength range of most commercially available emission filters are between 50 nm and 100 nm. This is not enough to distinguish the overlapping fluorescent proteins in our rainbow yeast strain, leaving more than one organelle in each channel of images [11].

4.1.4 Deep Learning in Biological Imaging and U-Net

Capturing the dynamics of the organelles requires the imaging system to do continuous timelapse, at a non-photodamaging light intensity, in a high frame rate, with a high spectral resolution. This is not achievable by either the spectral confocal microscopy or the filter cube-based widefield fluorescence microscopy. Therefore, we seek post-acquisition processing methods that take in images from one imaging system, and output images that also enjoy the advantages of the other system.

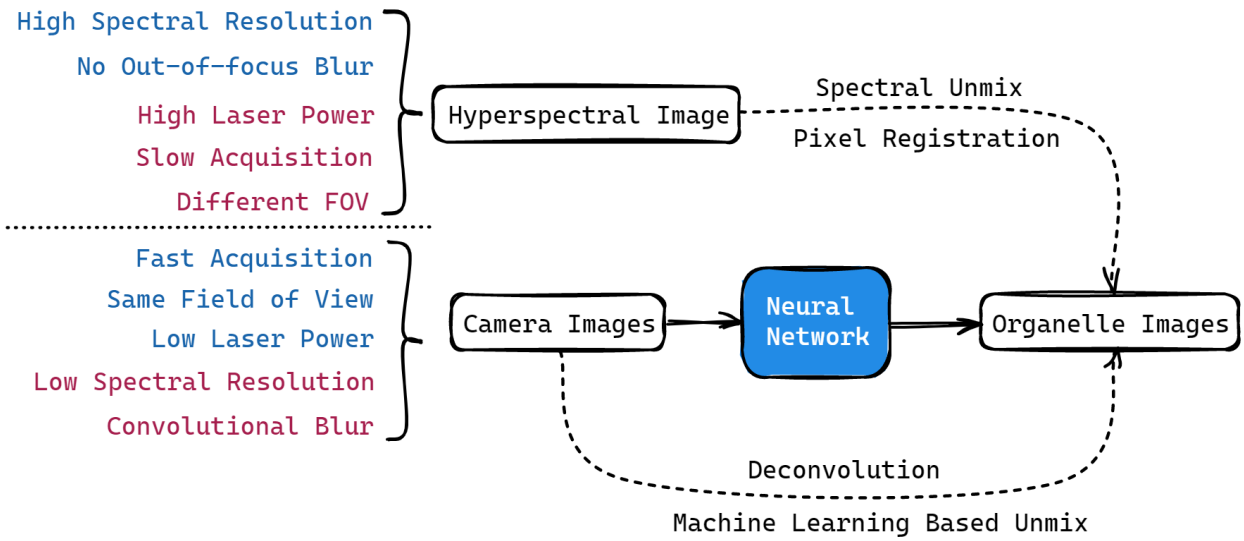

Figure 22 Illustration of the rationale of neural network training to combine the advantages of fluorescent microscopy and spectral confocal microscopy.

Machine learning is a class of algorithms that attempt to find the relationship between given input and output data [49]. Among them deep learning models use data structure and algorithms inspired from biological neural systems, and show great promises in image processing tasks [50]. U-Net is a deep learning network that was first developed to perform image segmentation [51]. Later studies have shown that the network can perform various other tasks by mutating network size and loss metrics [52].

To train a U-Net to perform our task, we need to take the images of the same rainbow yeast cells with both the sCMOS filtered fluorescent microscopy and the spectral confocal microscopy. The sCMOS filtered fluorescent microscopy serve as the training input. The training targets are either the raw images of the spectral confocal microscopy images, or images processed downstream of our previous image process workflow. When the training finishes, we have a model that can

segment different organelles into different color channels from the timelapse images taken by the sCMOS filtered fluorescent microscopy.

4.2 Methods

4.2.1 Image Acquisition

Both strains (EYrainbow wildtype) with and without a plasmid encoding a WHI5 overexpression construct (EYrainbow-Whi5up) were imaged. One day before imaging, the cells were transferred from petri dish colonies into 10 mL synthetic complete liquid medium and grew overnight. On the morning of imaging, the cells were diluted into OD (600 nm) = 0.1 and grew for another 3 hours to resume exponential growth. Then the cells were harvested with a centrifuge and made into a live microscope slide.

The microscope slide was observed under the Nikon Ti2 inverted microscope. After finding a field of view where the cells were dense but not overcrowded, the microscope was manually focused and locked in its Z position. Images were taken only at this Z position. The sCMOS camera images with proper fluorescent filters were taken before the spectral confocal microscopy images, in order to avoid photobleaching.

4.2.2 Image Registration

To register the fields of view between the sCMOS camera and the spectral detector, 0.1 μm TetraSpeck™ microspheres were imaged. The suspension beads were diluted 100 times in distilled water and thoroughly centrifuged. 2 uL diluted suspension was spread onto the microscope slide with a pipet tip and was left alone until the liquid dried out. Then we applied 2 uL synthetic complete media onto the bead area and covered it with covering glass. The slide was observed and focused under the microscope. Images of both the sCMOS camera and the spectral detector were taken.

After the image acquisition, we used ilastik to segment the beads from the background in the images. The correspondence between images of the same beads in different images were identified manually. The position of each bead is calculated from the coordinates of the segmented pixels, weighted by the pixel intensity in the original images. The affine transformations were calculated with the python scikit-image package [25].

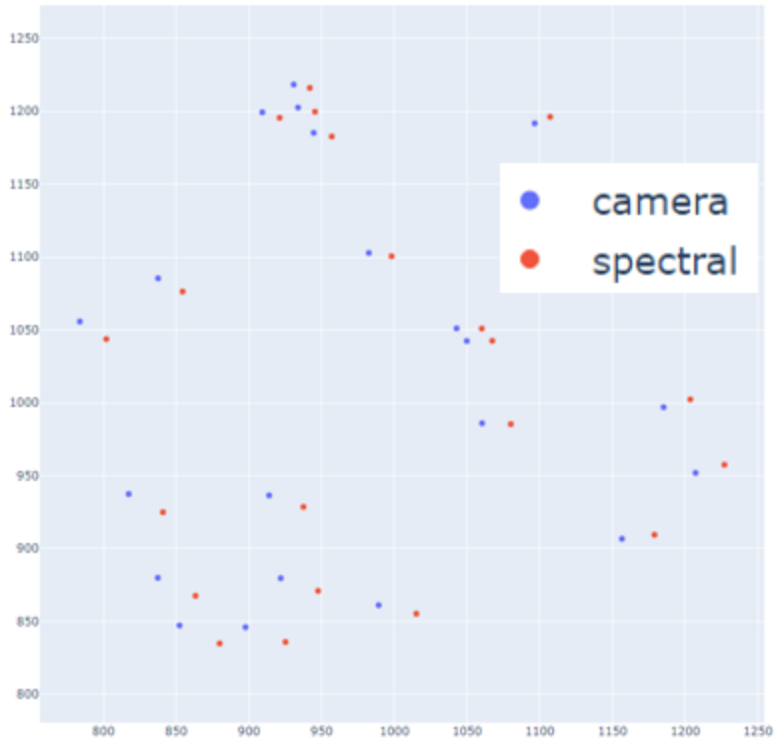

Figure 23 The comparison of the fields of view between the sCMOS camera and the spectral confocal detector. The dots are intensity weighted centroids of the microspheres.

The spectral images were transformed to align with the sCMOS camera images. This is because we want to keep the widefield microscopy images untransformed, so that the neural network could learn the unchanged morphology of organelles from the sCMOS camera images.

For a given 2-D coordinate $\vec{x}$ in the source image, its destiny coordinate $\vec{y}$ after an affine transformation can be expressed as $\vec{y} = A\vec{x} + \vec{b}$, where A is a similarity transform matrix, and $\vec{b}$ is a translation vector. Alternatively, it can be expressed with a 3-D matrix by appending coordinates with a 1:

$$\begin{bmatrix} \vec{y} \\ 1 \end{bmatrix} = \begin{bmatrix} A & \vec{b} \\ 0 \quad 0 & 1 \end{bmatrix} \begin{bmatrix} \vec{x} \\ 1 \end{bmatrix}$$

The 3-D affine transformation matrix from the spectral detector to the sCMOS camera with the cyan filter is:

$$\begin{bmatrix} 1.009527 & 0.04239949 & 224.4792 \\ -0.04500528 & 0.9778522 & 270.2124 \\ 0 & 0 & 1 \end{bmatrix}$$

The 3-D affine transformation matrix from the spectral detector to the sCMOS camera with the green filter is:

$$\begin{bmatrix} 1.009807 & 0.04264218 & 224.3990 \\ -0.04946186 & 0.9781828 & 270.6104 \\ 0 & 0 & 1 \end{bmatrix}$$

To apply the affine transformation from the spectral detector to the sCMOS camera without filters, the above two matrices were averaged.

4.2.3 Dataset Preparation

Registered images of all channels were cropped to 480 by 480 pixels around the center. The single-channel images were normalized between 0 and 1 with respect to the maximum and minimum of intensity. The channels that will serve as training inputs are saved into one multi-channel image file, and channels that will serve as training targets were saved as another multi-channel image file.

At the beginning of the training phase, the dataset was randomly split into a training set of 50 image pairs, and a validation set of 18 image pairs. In order to yield reproducible results, a random seed was selected.

4.2.4 U-Net Hyperparameters, and Training Environment

The U-Net is modified from the original version [51]. Contrary to the valid convolutions without padding, we padded the inputs to convolution with the boundary values, so that input and output of the neural network had the same size. This decouples the training phase from the data preparation phase, because valid convolution would change the size of output images, which requires re-configuration of the data loader when we change the U-Net model depth. And previous work has shown the same-size convolution does not compromise too much of the effectiveness of the neural network [52].

We also decreased the number of feature maps in every depth of the network, in order to reduce the size of the network and avoid overfitting. The effects of feature map numbers will be discussed in the result section. We chose the mean squared error as the loss function. The training batch size was 10 images. A total of 1500 epochs of training were performed. We saved the model that had the lowest loss on the validation set as the training result.

The training is performed on a high-performance computing cluster with operating-system-level virtualization. The training task was allocated with 16 GB CPU memory, and 16 GB GPU memory. By down tuning the batch size, this task is also able to run on personal workstations.

4.3 Results

4.3.1 Loss Function and its Descending on Training and Validation Datasets

The descending of loss between the trained model predictions and the ground truth had different behaviors on the training set and the validation set. (Figure 24) On the training set, the loss function kept getting lower values until the last epoch, while the loss recovered after around 1200 epochs on the validation set. This is an indication that the model is getting overfitted by the training set, i.e., it is learning common patterns among the images in the training set, that are not general morphological features of the corresponding organelles.

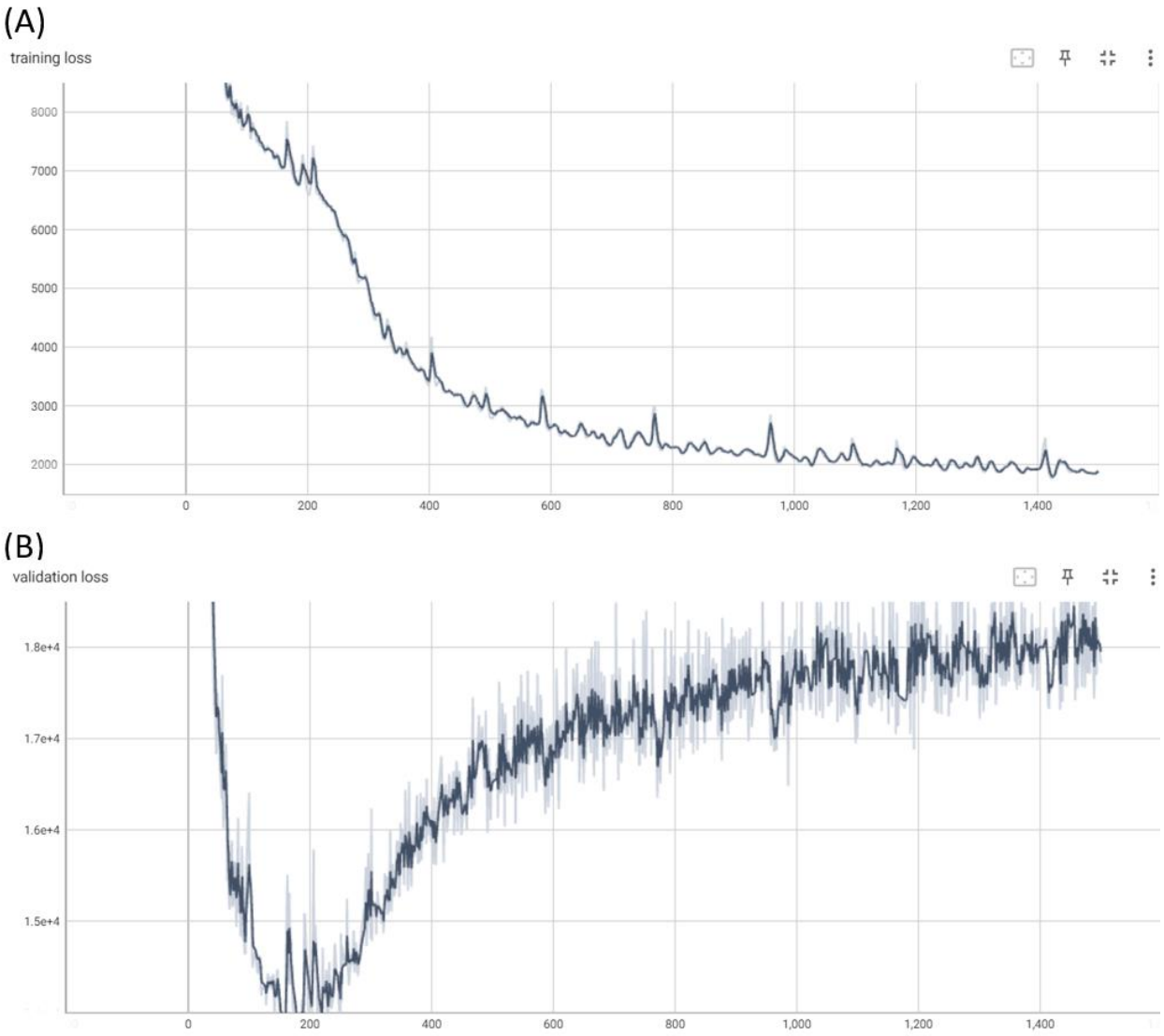

Figure 24 The loss between the model prediction and the ground truth, during 1500 epochs of training, in **(A)** the training dataset and **(B)** the validation dataset.

4.3.2 Comparison of Images between Model Prediction and Ground Truth

We first evaluated the training results by visually comparing the model predictions and the ground truth from the validation set. The model correctly picked the morphological structures that belonged to peroxisomes and endoplasm reticulum. We can also observe that the same organelle showed up at slightly different positions in the input image (sCMOS fluorescent

microscopy) and the ground truth (spectral confocal microscopy). This results from the movements of the organelles during the acquisition time difference of the two imaging. However, the recognition of vacuoles was not as promising, largely due to the low signal to noise ratio in both the training inputs and the training targets.

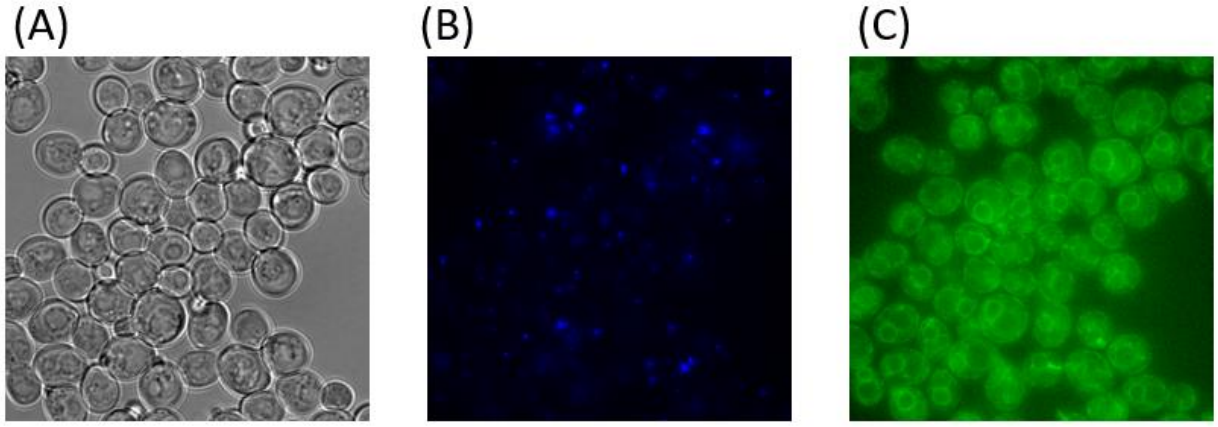

Figure 25 One group of bright field/fluorescent microscopy images, used as inputs into the neural network from the validation set. **(A)** bright field. **(B)** fluorescent microscopy with cyan filter. **(C)** fluorescent microscopy with green filter

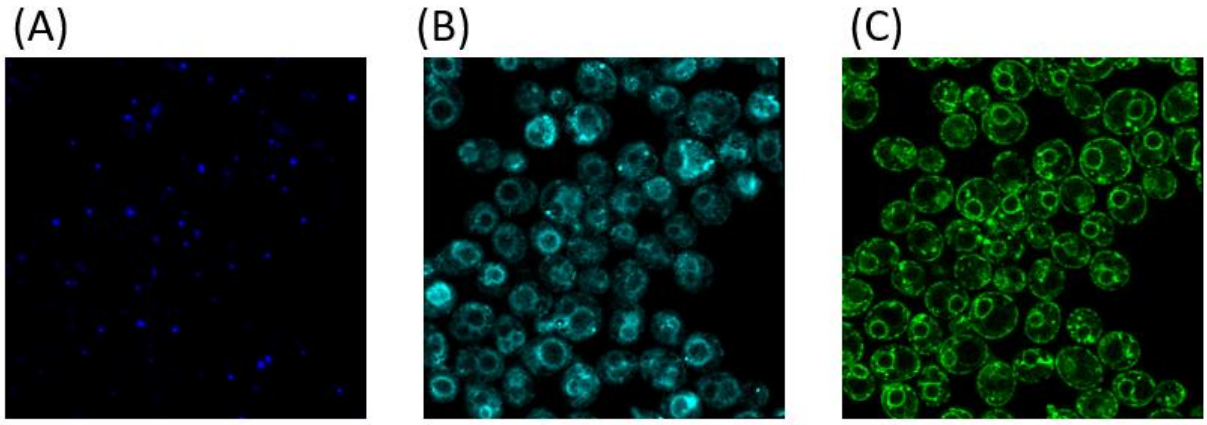

Figure 26 One group of ground truth of the neural network, for the same field of view as Figure 20, unmixed from the spectral confocal microscopy. **(A)** peroxisome. **(B)** vacuole. **(C)** endoplasm reticulum

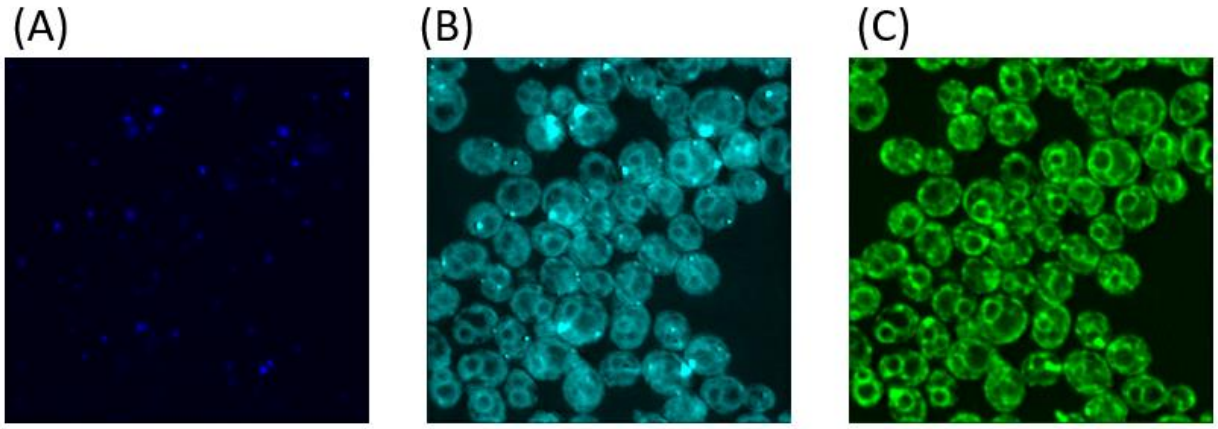

Figure 27 Predicted organelles as the output of the neural network, given the inputs as in Figure 25. **(A)** predicted peroxisome. **(B)** predicted vacuole. **(C)** predicted endoplasm reticulum.

4.3.3 Comparison of Extracted Statistics between Model Prediction and Ground Truth

In order to quantify the training results and find its applicability in the downstream research, we segmented images from both the ground truth images in the validation set, and corresponding model predictions, and compared the statistics extracted from the segmented images. We compared the total volumes of endoplasm reticulum in each cell, as well as the counting number of peroxisomes in each field of view. Both properties showed near 1 to 1 correspondence between the model prediction and the ground truth.

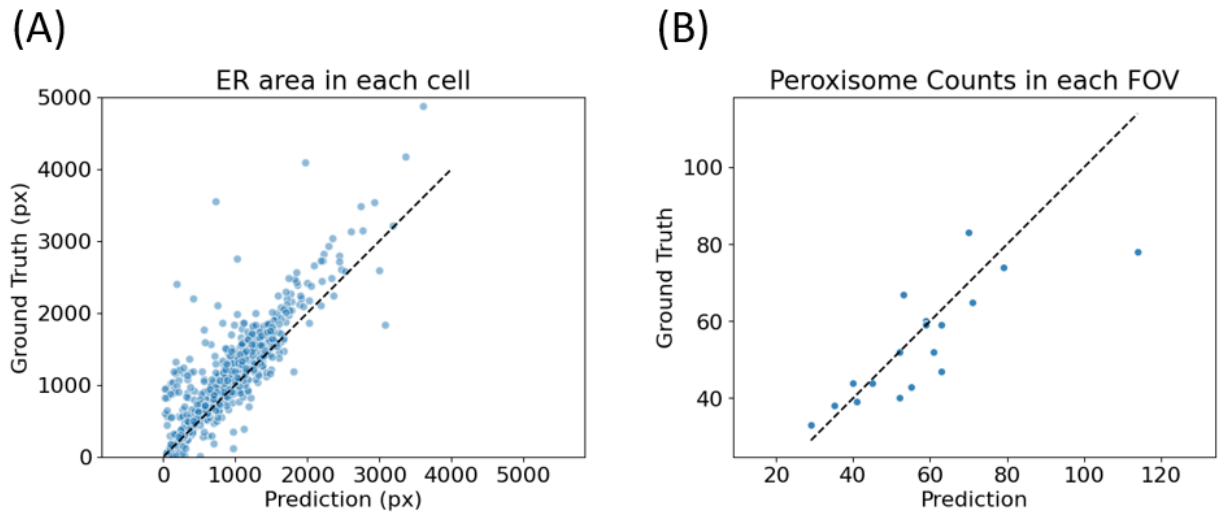

Figure 28 Comparison of statistics extracted from the predictions of the neural network and the ground truth. (A) the total area of endoplasm reticulum in each cell. (B) the counting number of peroxisomes in each field of view (FOV)

4.3.4 Segmentation training result from collaborators

To deal with the low signal-to-noise ratio problem in the vacuole images unmixed from the spectral confocal microscopy, I segmented the spectral images with ilastik [28]. By using this segmented organelle images as the training target, we a turning the original image translation task into an image segmentation task, which is also what U-Net has proven to be effective.

Our collaborators Gabi Wurgaft, Shirin Shoushtari, Yuyang Hu, and Ulugbek Kamilov trained a different U-Net with our sCMOS camera images and the segmented organelle images. The number of initial feature maps was 32, while our model is 8. They cropped the input and target images to 180 by 180 pixels to increase the number of images in the dataset, so that the increase in the feature map number would not cause overfitting. They also reduced the overfitting by decreasing the depth of the U-Net from 5 to 4. (Figure 29) Peak signal-to-noise ratio (PSNR),

signal-to-noise ratio (SNR), and structural similarity index (SSIM) were combined to evaluate the loss between the neural network prediction and the ground truth.

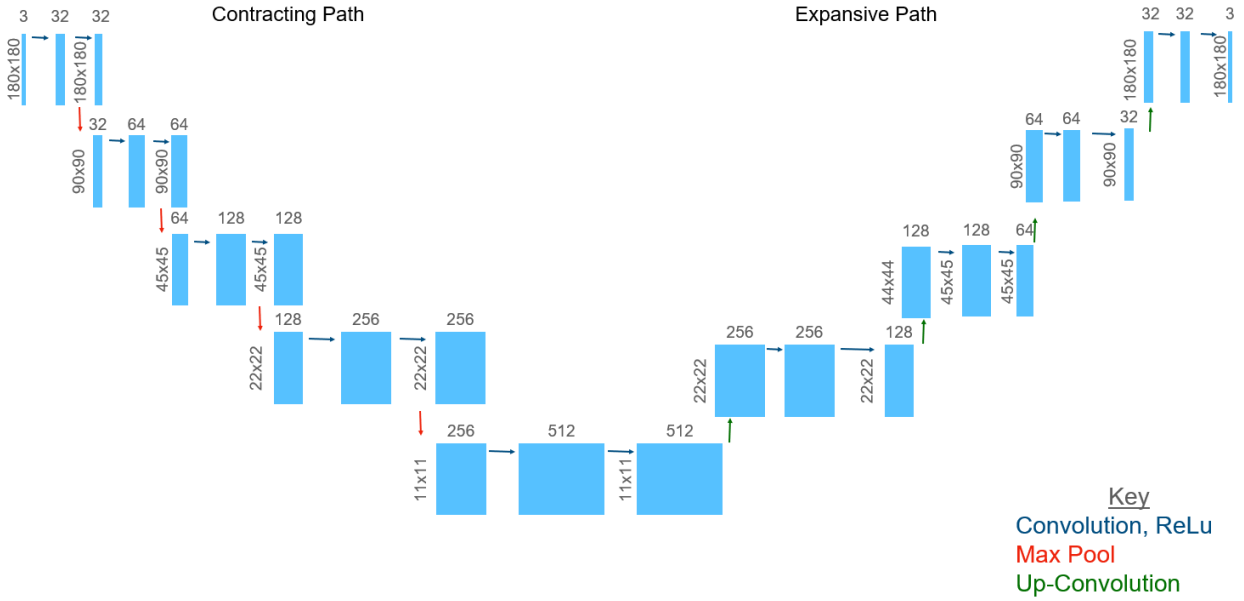

Figure 29 Model structure of the improved U-Net by Gabi Wurgaft, Shirin Shoushtari, Yuyang Hu, and Ulugbek Kamilov

Figure 30 shows the model input, the prediction from the neural network, and the ground truth of a member of the validation dataset. (Figure 30) The PSNR is 13.75, the SNR is 3.087, and SSIM is 0.151, which are unusually low. However, the prediction from the neural network correctly captures the morphological features of the organelles, although the intensity of the predicted images is significantly lower than the ground truth.

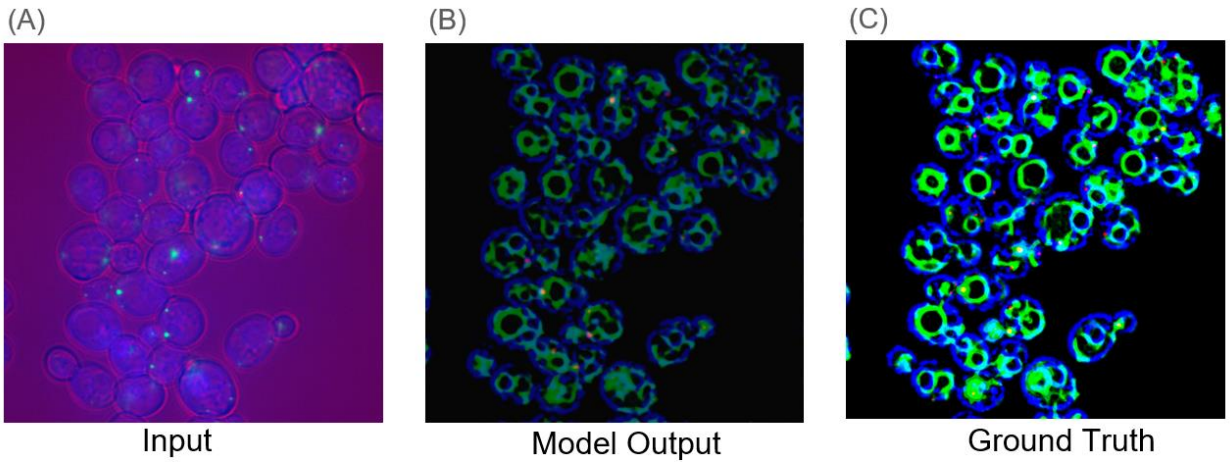

Figure 30 comparison of the input to the improved U-Net **(A)**, the prediction from the network **(B)**, and the ground truth **(C)**. by Gabi Wurgaft, Shirin Shoushtari, Yuyang Hu, and Ulugbek Kamilov

4.4 Discussion

The findings of this research project revealed the efficacy of the trained U-Net model in accurately segmenting and identifying organelles. Visual examination of the model predictions against the ground truth from the validation set demonstrated precise identification of peroxisomes and endoplasmic reticulum structures. However, the recognition of vacuoles was hindered by the limitations posed by the low signal-to-noise ratio in both the training inputs and targets. Moreover, quantitative analysis comparing the extracted statistics from the model predictions and ground truth indicated a close correspondence between the two for the total volumes of endoplasmic reticulum and the counting number of peroxisomes.

The observed disparities in the descent of the loss function between the training and validation datasets provided insights into the potential issue of overfitting. This phenomenon, together with the image quality issue in the vacuole images, suggests that a training dataset of a larger size and a higher signal-to-noise ratio is a most urgent requirement to improve this technique.

In conclusion, this research project integrated advanced imaging techniques and deep learning analysis to investigate the dynamic regulation of organelles in yeast cells. The utilization of

confocal microscopy, spectral imaging, and sCMOS camera imaging could provid valuable insights into the dynamics of organelles. The trained U-Net model demonstrated accurate segmentation and recognition of organelles, despite encountering challenges such as a low signal-to-noise ratio and the potential for overfitting. Future research endeavors should focus on enhancing the robustness of the model and exploring additional image processing and analysis techniques to further advance our understanding of organelle dynamics and their regulatory mechanisms in cellular growth processes.

Chapter 5: Conclusion

In this thesis, we have undertaken a comprehensive exploration of organelle dynamics and their regulatory mechanisms in cellular growth processes. By combining advanced imaging techniques, including confocal microscopy, spectral imaging, and sCMOS camera imaging, with deep learning analysis using the U-Net model, we have made strides in understanding the regulation of organelles in yeast cells, and made promising progress in developing tools to understand their dynamics.

Our findings reveal that the systems-level organelle biogenesis program is composed of collective organelle modes that respond to changes in nutrient availability. Through chemical biological dissection, we demonstrate that distinct organelle modes are specifically activated by the sensed growth rate and size of the cell, orchestrating the cellular organelle-scale response to environmental cues. Mathematical modeling and synthetic biological control further suggest that these distinct organelle modes enable the cell to maintain robust growth homeostasis while remaining responsive to varying environmental conditions. This regulatory architecture likely underlies the eukaryotic cell's ability to flexibly adjust cell sizes and growth rates, accommodating diverse environmental and developmental constraints [11].

We also enhance our understanding of how cells allocate resources to different organelles for growth purposes using quantitative models. The model explores the resource allocation process in cells and investigates how signals related to cell size and growth rate affect organelle distribution. In this model, excess volume is assigned to vacuoles to maintain a consistent

nucleocytoplasmic volume fraction, and experimental evidence using PopTag supports this concept [12].

By elucidating the principles governing organelle biogenesis and cellular growth, our research contributes to a deeper understanding of fundamental cellular processes. Moreover, this knowledge has implications for various fields, including biotechnology, medicine, and synthetic biology. By comprehensively examining the interplay between organelles and cellular growth, we lay the foundation for future research endeavors that seek to unravel the complexities of eukaryotic cells and their regulatory mechanisms [11, 12].

Our research demonstrated the efficacy of the trained U-Net model in accurately segmenting and identifying organelles. Visual examination and quantitative analysis confirmed the model's ability to precisely identify peroxisomes and endoplasmic reticulum structures. However, challenges were encountered in recognizing vacuoles due to the limitations posed by low signal-to-noise ratios in both the training inputs and targets. We identified the need for larger training datasets with higher signal-to-noise ratios as an urgent requirement to improve this technique and address potential overfitting issues.

The integration of advanced imaging techniques and deep learning analysis has provided valuable insights into the dynamics of organelles. By uncovering the correlation structure of systems-level organelle biogenesis with cellular growth, we have shed light on the collective organelle modes activated by changes in nutrient availability. The activation of these distinct organelle modes, driven by the sensed growth rate and size of the cell, allows for the

maintenance of robust growth homeostasis while enabling responsiveness to varying environmental cues.

While our research has significantly advanced our understanding of organelle dynamics and regulation, there remain avenues for further exploration. Enhancing the robustness of the U-Net model and exploring additional image processing and analysis techniques can contribute to a deeper understanding of organelle dynamics. Furthermore, investigating the interplay between organelles and other cellular processes, such as gene expression and signal transduction, holds great potential for unraveling the complexities of eukaryotic cells.

In conclusion, this thesis represents a significant step forward in our understanding of organelle biogenesis, cellular growth, and their regulatory mechanisms in eukaryotic cells. The insights gained through our research provide a solid foundation for future studies that seek to uncover the intricacies of cellular organization and function. By continuing to explore and unravel the mysteries of organelles, we can unlock new avenues for advancements in biotechnology, medicine, and our understanding of life itself.

References

[1] Alberts B, Bray D, Hopkin K, Johnson AD, Lewis J, Raff M, Roberts K, Walter P., Essential cell biology, Garland Science, 2015.

[2] Chan, Yee-Hung M and Marshall, Wallace F, "How cells know the size of their organelles," *Science,* vol. 337, pp. 1186-1189, 2012.

[3] Levy, Daniel L and Heald, Rebecca, "Mechanisms of intracellular scaling," *Annual review of cell and developmental biology,* vol. 28, pp. 113-35, 2012.

[4] Goehring, Nathan W and Hyman, Anthony A, "Organelle growth control through limiting pools of cytoplasmic components," *Current Biology,* vol. 22, no. 9, pp. R330-R339, 2012.

[5] Jorgensen P, Edgington NP, Schneider BL, Rupes I, Tyers M, Futcher B, "The size of the nucleus increases as yeast cells grow," *Molecular biology of the cell,* vol. 18, no. 9, pp. 3523-3532, 2007.

[6] Mukherjee RN, Sallé J, Dmitrieff S, Nelson KM, Oakey J, Minc N, Levy DL, "The perinuclear ER scales nuclear size independently of cell size in early embryos," *Developmental cell,* vol. 54, no. 3, pp. 395-409, 2020.

[7] M. W. Chan YH, "Organelle size scaling of the budding yeast vacuole is tuned by membrane trafficking rates," *Biophysical journal,* vol. 106, no. 9, pp. 1986-1996, 2014.

[8] Rafelski, Susanne M and Viana, Matheus P and Zhang, Yi and Chan, Yee-Hung M and Thorn, Kurt S and Yam, Phoebe and Fung, Jennifer C and Li, Hao and Costa, Luciano da F and Marshall, Wallace F, "Mitochondrial network size scaling in budding yeast," *Science,* vol. 338, no. 6108, pp. 822-824, 2012.

[9] Miettinen TP, Björklund M, "Mitochondrial function and cell size: an allometric relationship," *Trends in cell biology,* vol. 27, no. 6, pp. 393-402, 2017.

[10] Gottschling DE, Nyström T, "The Upsides and Downsides of Organelle Interconnectivity," *Cell,* vol. 169, no. 1, pp. 24-34, 2017.

[11] Wang, Shixing and Mukherji, Shankar, "Uncovering the principles coordinating systems-level organelle biogenesis with cellular growth," *bioRxiv,* pp. 2022--11, 2022.

[12] Wang, Shixing, Kailash, Deepthi, and Mukherji, Shankar, "Uncovering the principles coordinating systems-level organelle biogenesis with cellular growth," *Manuscript in preparation,* 2023.

[13] Metzl-Raz, Eyal, Moshe Kafri, Gilad Yaakov, Ilya Soifer, Yonat Gurvich, and Naama Barkai, "Principles of cellular resource allocation revealed by condition-dependent proteome profiling," *Elife .,* vol. 6, no. e28034, 2017.

[14] Viana, Matheus P and Chen, Jianxu and Knijnenburg, Theo A and Vasan, Ritvik and Yan, Calysta and Arakaki, Joy E and Bailey, Matte and Berry, Ben and Borensztejn, Antoine and Brown, Jackson M, "Robust integrated intracellular organization of the human iPS cell: where, how much, and how variable," *BioRxiv,* pp. 2020--12, 2020.

[15] Uchida, Maho and Sun, Yidi and McDermott, Gerry and Knoechel, Christian and Le Gros, Mark A and Parkinson, Dilworth and Drubin, David G and Larabell, Carolyn A, "Quantitative analysis of yeast internal architecture using soft X-ray tomography," *Yeast,* vol. 38, no. 3, pp. 227--236, 2011.

[16] Xu, C Shan and Pang, Song and Shtengel, Gleb and Müller, Andreas and Ritter, Alex T and Hoffman, Huxley K and Takemura, Shin-ya and Lu, Zhiyuan and Pasolli, H Amalia and Iyer, Nirmala, "An open-access volume electron microscopy atlas of whole cells and tissues," *Nature,* vol. 599, no. 7883, pp. 147--151, 2021.

[17] Chan, Yee-Hung M and Reyes, Lorena and Sohail, Saba M and Tran, Nancy K and Marshall, Wallace F, "Organelle size scaling of the budding yeast vacuole by relative growth and inheritance," *Current Biology,* vol. 26, no. 9, pp. 1221-1228, 2016.

[18] Huh, Won-Ki and Falvo, James V and Gerke, Luke C and Carroll, Adam S and Howson, Russell W and Weissman, Jonathan S and O'Shea, Erin K, "Global analysis of protein localization in budding yeast," *Nature,* vol. 425, no. 6959, pp. 686--691, 2003.

[19] Mukherji, Shankar and O'Shea, Erin K, "Mechanisms of organelle biogenesis govern stochastic fluctuations in organelle abundance," *Elife,* vol. 3, p. e02678, 2014.

[20] Sheff, Mark A and Thorn, Kurt S, "Optimized cassettes for fluorescent protein tagging in Saccharomyces cerevisiae," *Yeast,* vol. 21, no. 8, pp. 661--670, 2004.

[21] Zhu, Jing and Zhang, Zheng-Tan and Tang, Shi-Wei and Zhao, Bo-Song and Li, Hui and Song, Jing-Zhen and Li, Dan and Xie, Zhiping, "A validated set of fluorescent-protein-based markers for major organelles in yeast (Saccharomyces cerevisiae)," *Molecular Biology,* vol. 10, no. 5, pp. 10--1128, 2019.

[22] Lee, Sidae and Lim, Wendell A and Thorn, Kurt S, "Improved blue, green, and red fluorescent protein tagging vectors for S. cerevisiae," *PloS one,* vol. 8, no. 7, p. e67902, 2013.

[23] Jorgensen, Paul and Nishikawa, Joy L and Breitkreutz, Bobby-Joe and Tyers, Mike, "Systematic identification of pathways that couple cell growth and division in yeast," *Science,* vol. 297, no. 5580, pp. 395--400, 2002.

[24] T. Lambert, "FPbase: a community-editable fluorescent protein database," *Nature Methods,* vol. 16, p. 277–278, 2019.

[25] Van der Walt, Stefan and Schönberger, Johannes L. and Nunez-Iglesias, Juan and Boulogne, Fran{\c{c}}ois and Warner, Joshua D. and Yager, Neil and ... and Yu, Ting, "scikit-image: image processing in Python," *PeerJ,* vol. 2, p. e453, 2014.

[26] Dietler, N. and Minder, M. and Gligorovski, V. and Economou, AM. and Joly, DA. and Sadeghi, A. and Chan, CH. and Koziński, M. and Weigert, M. and Bitbol, AF. and Rahi, SJ., "A convolutional neural network segments yeast microscopy images with high accuracy," *Nature communications,* vol. 11, no. 1, p. 5723, 2020.

[27] Abramoff, Michael D. and Magalhaes, Pedro J. and Ram, Sohini J., "Image Processing with ImageJ," *Biophotonics International,* vol. 11, no. 7, pp. 36-42, 2004.

[28] Berg, Stuart and Kutra, Dominik and Kroeger, Thorben and Straehle, Christoph N. and Kausler, Bernhard X. and Haubold, Carsten and Schiegg, Martin and Ales, Janez and Beier, Thorsten and Rudy, Markus and Eren, Kemal and Cervantes, Jaime I. and Xu, Buote an, "ilastik: interactive machine learning for (bio)image analysis," *Nature Methods,* 2019.

[29] Kullback, Solomon and Leibler, Richard A, "On information and sufficiency," *The annals of mathematical statistics,* vol. 22, no. 1, pp. 79--86, 1951.

[30] Aoh, Quyen L and Graves, Lee M and Duncan, Mara C, "Glucose regulates clathrin adaptors at the trans-Golgi network and endosomes," *Molecular biology of the cell,* vol. 22, no. 19, pp. 3671--3683, 2011.

[31] Jorgensen, Paul and Rupes, Ivan and Sharom, Jeffrey R and Schneper, Lisa and Broach, James R and Tyers, Mike, "A dynamic transcriptional network communicates growth potential to ribosome synthesis and critical cell size," *Genes & development,* vol. 18, no. 20, pp. 2491--2505, 2004.

[32] Kellogg, Douglas R and Levin, Petra Anne, "Nutrient availability as an arbiter of cell size," *Trends in Cell Biology,* 2022.

[33] Johnston, GC and Ehrhardt, CW and Lorincz, A and Carter, BL, "Regulation of cell size in the yeast Saccharomyces cerevisiae," *Journal of bacteriology,* vol. 137, no. 1, pp. 1--5, 1979.

[34] Fantes, P and Nurse, P, "Control of cell size at division in fission yeast by a growth-modulated size control over nuclear division," *Experimental cell research,* vol. 107, no. 2, pp. 377--386, 1977.

[35] Ferrezuelo, Francisco and Colomina, Neus and Palmisano, Alida and Gar{\'\i}, Eloi and Gallego, Carme and Csikász-Nagy, Attila and Aldea, Martí, "The critical size is set at a single-cell level by growth rate to attain homeostasis and adaptation," *Nature communications,* vol. 3, no. 1, p. 1012, 2012.

[36] Leitao, Ricardo M and Kellogg, Douglas R, "The duration of mitosis and daughter cell size are modulated by nutrients in budding yeast," *Journal of Cell Biology,* vol. 216, no. 11, pp. 3463--3470, 2017.

[37] Goranov, Alexi I and Cook, Michael and Ricicova, Marketa and Ben-Ari, Giora and Gonzalez, Christian and Hansen, Carl and Tyers, Mike and Amon, Angelika, "The rate of cell growth is governed by cell cycle stage," *Genes & development,* vol. 23, no. 12, pp. 1408--1422, 2009.

[38] Schmoller, Kurt M and Turner, JJ and Köivomägi, M and Skotheim, Jan M, "Dilution of the cell cycle inhibitor Whi5 controls budding-yeast cell size," *Nature,* vol. 526, no. 7572, pp. 268--272, 2015.

[39] Arita, Yuko and Kim, Griffin and Li, Zhijian and Friesen, Helena and Turco, Gina and Wang, Rebecca Y and Climie, Dale and Usaj, Matej and Hotz, Manuel and Stoops, Emily H, "A genome-scale yeast library with inducible expression of individual genes," *Molecular Systems Biology,* vol. 17, no. 6, p. e10207, 2021.

[40] Boer, Viktor M and Amini, Sasan and Botstein, David, "Influence of genotype and nutrition on survival and metabolism of starving yeast," *Proceedings of the National Academy of Sciences,* vol. 105, no. 19, pp. 6930--6935, 2008.

[41] Kunkel, Joseph and Luo, Xiangxia and Capaldi, Andrew P, "Integrated TORC1 and PKA signaling control the temporal activation of glucose-induced gene expression in yeast," *Nature communications,* vol. 10, no. 1, p. 3558, 2019.

[42] Zaman, Shadia and Lippman, Soyeon Im and Zhao, Xin and Broach, James R, "How Saccharomyces responds to nutrients," *Annual review of genetics,* vol. 42, pp. 27--81, 2008.

[43] Hao, Nan and Budnik, Bogdan A and Gunawardena, Jeremy and O'Shea, Erin K, "Tunable signal processing through modular control of transcription factor translocation," *Science,* vol. 339, no. 6118, pp. 460--464, 2013.

[44] Barrett, Harrison H and Myers, Kyle J, Foundations of image science, John Wiley & Sons, 2013.

[45] P. Bankhead, "Analyzing fluorescence microscopy images with ImageJ," *ImageJ,* vol. 1, no. 195, pp. 10--1109, 2014.

[46] J. Pawley, Handbook of biological confocal microscopy, vol. 236, Springer Science & Business Media, 2006.

[47] T. Zimmermann, "Spectral imaging and linear unmixing in light microscopy," *Microscopy Techniques,* pp. 245--265, 2005.

[48] J. Wallace, "Photonics products: Scientific CMOS cameras: sCMOS cameras reach new levels of capability," *Laser Focus World,* 2018.

[49] Jordan, Michael I and Mitchell, Tom M, "Machine learning: Trends, perspectives, and prospects," *Science,* vol. 349, no. 6245, pp. 255--260, 2015.

[50] LeCun, Yann, Yoshua Bengio, and Geoffrey Hinton, "Deep learning," *nature* , vol. 521, no. 7553, pp. 436-444, 2015.

[51] Ronneberger, Olaf and Fischer, Philipp and Brox, Thomas, "U-net: Convolutional networks for biomedical image segmentation," in *Medical Image Computing and Computer-Assisted Intervention--MICCAI 2015: 18th International Conference, Munich, Germany, October 5-9, 2015, Proceedings, Part III,* 2015.

[52] Chawin Ounkomol and Sharmishtaa Seshamani and Mary M. Maleckar and Forrest Collman and Gregory R. Johnson, "Label-free prediction of three-dimensional fluorescence images from transmitted-light microscopy," *Nature Methods,* vol. 15, no. 11, pp. 917--920, 2018.